Lightweight design of variable-angle filament-wound cylinders combining Kriging–based metamodels with particle swarm optimization

Zhihua Wang[a,b], José Humberto S. Almeida Jr.[c,d,*], Aravind Ashok[a], Zhonglai Wang[b,*] and Saullo G. P. Castro[a,*]

[a]Faculty of Aerospace Engineering, Delft University of Technology, Delft, The Netherlands
[b]School of Mechanical and Electrical Engineering, University of Electronic Science and Technology of China, Chengdu, China
[c]Department of Mechanical Engineering, Aalto University, Espoo, Finland
[d]Advanced Composites Research Group, School of Mechanical and Aerospace Engineering, Queen's University Belfast, UK

ARTICLE INFO

Keywords:
Mass minimization
Metamodeling
Variable stiffness
variable-angle
filament winding
buckling

ABSTRACT

Variable–angle filament–wound (VAFW) cylinders are herein optimized for minimum mass under manufacturing constraints, and for various design loads. A design parameterization based on a second–order polynomial variation of the tow winding angle along the axial direction of the cylinders is utilized to explore the nonlinear steering–thickness dependency in VAFW structures, whereby the thickness becomes a function of the fiber angle. Particle swarm optimization coupled with several Kriging-based metamodels is developed to find the optimum designs. A single–curvature Bogner-Fox-Schmit-Castro finite element is formulated to accurately and efficiently represent the variable stiffness properties of the shells, and verifications are performed using a general–purpose plate element. Alongside the main optimization studies, a vast analysis on the design space is performed using the metamodels, showing a gap in the design space for the buckling strength that is confirmed by genetic algorithm optimizations. Extreme lightweight whilst buckling resistant designs are found, along with non–conventional optimum layouts thanks to the high degree of thickness build–up tailoring.

1. Introduction

The development of new concepts for lightweight structures has been overwhelmingly exploited in several fields, mainly in aeronautical and aerospace structures, to comply with Green Aviation for enhancing fuel efficiency and decrease aviation emissions towards reaching carbon–neutral air transportation. A practical and direct manner to improve the energy efficiency and reduce the fuel consumption of an aircraft is by reducing the mass of its components [1]. Achieving as a direct consequence carbon footprint reduction and better flight performance. Both aeronautical and space industries have been continuously developing new concepts for lightweight structures to pursue these benefits, where fiber-reinforced composite materials play a major role. Figure 1 illustrates the evolution of the use of composites in aeronautics over the last 60 decades.

In 2017, NASA designed, optimized, manufactured and tested a variable-angle tow (VAT) wing for optimal passive load alleviation, proving that the use of fiber steering through automated fiber placement (AFP) manufacturing is more structurally efficient than conventional straight–fiber–reinforced composite wings [2].
Liguori et al. [3] optimized a wingbox section using genetic algorithms, including manufacturing constraints pertaining AFP manufacturing, achieving a wingbox section that was 6.48% lighter, with higher buckling strength and reduced out-of-plane displacement in the post-buckled regime, when compared with the initial straight-fiber baseline structure. In fact, tailoring a particular property for laminated composites by means of in–plane point–wise fiber angle changing is proven to be efficient, already since the very first report from Hyer and Lee (1991) [4] on variable-angle tow (VAT) configurations, with the aim to optimize the buckling capacity of simply–supported open–hole laminates in uni-axial compression. Thenceforth, several approaches have been developed based on the advancement of both computational approaches and manufacturing techniques for composite materials.

Modern aircraft have their fuselages made of carbon fiber reinforced polymer (CFRP) composites, which makes cylindrical unstiffened shells [5] of particular importance towards understanding and further reducing aircraft overall mass. In spacecraft, monocoque structures are commonly built of unstiffened shells, requiring conservative knock-down factors to account for the high sensitivity of the buckling strength towards geometric and load imperfections [6]. The full potential of CFRP composites in these components is still under–explored, and an efficient strategy to take full advantage of these materials consists of reducing their masses whilst keeping their structural performance. The state–of–the–art on mass minimization of composite shells is scarce, as discussed next, with most of the studies focusing on optimization problems that seek minimum compliance for a given

*Corresponding Authors
zhwanglbb@gmail.com (Z. Wang); humberto.almeida@aalto.fi (J.H.S. Almeida Jr.); A.Ashok-2@student.tudelft.nl (A. Ashok); wzhonglai@uestc.edu.cn (Z. Wang); S.G.P.Castro@tudelft.nl (S.G.P. Castro)
ORCID(s): 0000-0001-8930-4817 (Z. Wang); 0000-0002-9408-7674 (J.H.S. Almeida Jr.); 0000-0002-6587-3107 (A. Ashok); 0000-0002-1708-4197 (Z. Wang); 0000-0001-9711-0991 (S.G.P. Castro)

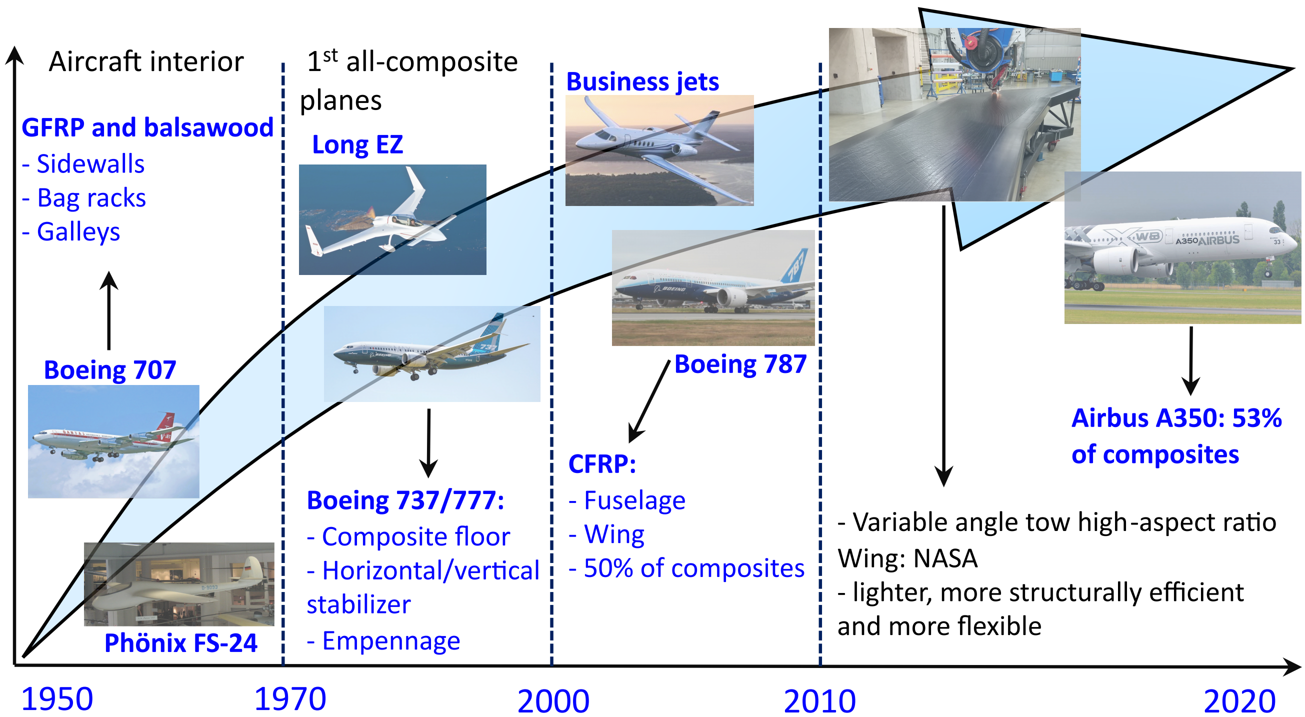

Figure 1: Utilization of fiber–reinforced composites in aircraft over the last decades.

mass. Pelletier and Vel [7] developed a multi-objective optimization of composite cylinders for strength, stiffness and minimal mass via the layerwise tailoring of fiber angles and fiber volume fraction. Although some enhancements were found, it was difficult to find a layout with reasonable compromise among the three objective functions utilized. Sadeghifar et al. [8] optimized stiffened cylindrical shells for minimum mass and maximum axial buckling load using a genetic algorithm (GA), finding that I-section stiffeners are more effective than rectangular ones to achieve panels with reduced mass. Ghasemi and Hajmohammad [9] proposed a multi-objective optimization of composite shells under external pressure for minimum mass and maximum buckling pressure using GA. They reached a mass reduction of 12% while respecting the desired buckling pressure.

In general, optimizations based on GA require thousands of function evaluations, becoming therefore limited due to the high computational cost. An appropriate strategy to improve the efficiency of these optimizations is to employ metamodels, which are computationally efficient surrogate models that approximate the high-fidelity response using approximated functions, such as hyper-surfaces. Rouhi et al. [10] optimized VAT cylindrical shells for maximum buckling load using radial basis functions as surrogates and genetic algorithms to find the optimum in the surrogate model. Blom et al. [11] used design explorer tools [12] as surrogates to minimize the buckling load of VAT composite cylinders. Recently, Wang et al. [13] developed a new accelerated Kriging metamodeling scheme to restrict the area of interest within an optimization framework to maximize the buckling load of VAT composite cylinders manufactured by filament winding, designated as variable–angle filament–wound – VAFW.

No work on minimizing mass for VAT composite cylinders has been found, especially using manufacturing constraints from filament winding (FW), which is the most suitable and fastest manufacturing process for composite cylinders [14]. To fulfil this gap, the present work proposes an optimization approach to minimize the mass of VAFW cylinders, constrained by design loads for uni-axial buckling strength. Three Kriging–based metamodels are developed and assessed to be used in the optimizations, namely: Kriging, Co-Kriging, and Accelerated–Kriging. The finite element analysis are performed using a single-curvature Bogner-Fox-Schmit-Castro (BFSC) [15], consisting of an enriched rectangular four–node element with ten degrees–of–freedom per node to achieve third–order interpolation for the displacement field. The FE model takes into consideration the manufacturing characteristics of the FW process, and can accurately represent the varying stiffness properties of the proposed design parameterization. The FE predictions from the single–curvature BFSC model for different design loads are verified against a general purpose shell element of a commercial FE software. A vast analysis on the design space is performed using Kriging–based metamodels, showing the ranges of mass and buckling strength for different number of layers. The possible mass range for different design loads is also shown, and the optimal configurations

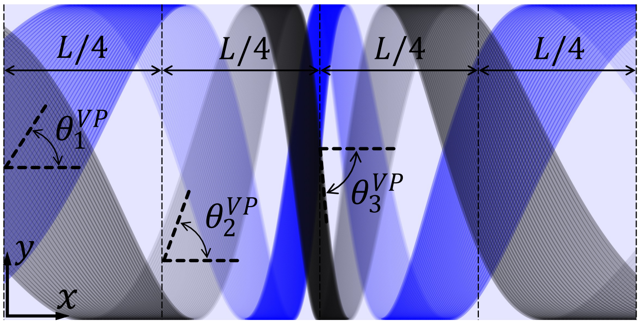

Figure 2: VAFW-P parameterization with three design variables θ_1^{VP}, θ_2^{VP} and θ_2^{VP} per angle–ply layer consisting of two plies with winding angle distribution $\pm\theta(x)$.

are verified against a conventional genetic algorithm (GA) optimization.

2. The design

The pioneering work of Wang et al. [13] on reliability-based design optimization of variable–angle filament–wound (VAFW) cylinders, compared different VAFW designs and found that the maximum buckling load was achieved by the design named VAFW-P, whose winding angle distribution $\theta(x)$ varies along the longitudinal direction using a second-order Lagrange polynomial [16], as given in Eq. 1. Each angle–ply layer consisting of two plies of angles $\pm\theta(x)$ is controlled by three design variables θ_1^{VP}, θ_2^{VP} and θ_3^{VP}; whose control points are fixed at $x_1 = 0$, $x_2 = L/4$, $x_3 = L/2$, $x_4 = 3L/4$, $x_5 = L$, as shown in Figure 2. In the present work, the VAFW-P parameterization is used to find optimum designs of minimum mass for different design load levels, whereby the number of angle–ply layers and the winding angle distribution in each layer are the design variables to be determined.

$$\theta(x) = \begin{cases} N_1\theta_1^{VP} + N_2\theta_2^{VP} + N_3^L\theta_3^{VP}, & x \le \frac{L}{2} \\ N_3^R\theta_3^{VP} + N_4\theta_2^{VP} + N_5\theta_1^{VP}, & x > \frac{L}{2} \end{cases} \tag{1}$$

where:

$$\begin{aligned} N_1 &= \frac{(x-x_2)(x-x_3)}{(x_1-x_2)(x_1-x_3)}; & N_2 &= \frac{(x-x_1)(x-x_3)}{(x_2-x_1)(x_2-x_3)} \\ N_3^L &= \frac{(x-x_1)(x-x_2)}{(x_3-x_1)(x_3-x_2)}; & N_3^R &= \frac{(x-x_4)(x-x_5)}{(x_3-x_4)(x_3-x_5)} \\ N_4 &= \frac{(x-x_3)(x-x_5)}{(x_4-x_3)(x_4-x_5)}; & N_5 &= \frac{(x-x_3)(x-x_4)}{(x_5-x_3)(x_5-x_4)} \end{aligned} \tag{2}$$

As explained in Wang et al [13], for VAFW cylinders the thickness distribution of the k^{th} ply given by $h_k(x)$ changes due to filament bending, filament shearing or any combination of both [13], and the thickness increase is necessary to keep a constant volume [17, 18], leading to the following nonlinear dependence of $h_k(x)$ with the winding angle distribution $\theta(x)$:

$$h_k(x) = \frac{h_{tow}}{\cos\Delta\theta(x)} \tag{3}$$

with h_{tow} being the filament thickness; the filament steering angle is calculated simply by $\Delta\theta(x) = \theta(x) - \min(\theta(x))$, for $0 \le x \le L$. The steering-thickness coupling of Eq. 3 poses yet another challenge for the design and optimization, where the mass of VAFW cylinders becomes not only a function of the number of angle–ply layers, but also depends on the winding angle distribution $\theta(x)$. The geometry of all cylinders herein optimized is fixed, with a radius of $r = 0.15$ m, and length of $L = 0.3$ m. The orthotropic material properties of the filaments are: $E_{11} = 90$ GPa, $E_{22} = 7$ GPa, $\nu_{12} = 0.32$, $G_{12} = G_{13} = G_{23} = 4.4$ GPa; with a filament thickness of $h_{tow} = 0.4$ mm. The material density is $\rho = 1600 kg/m^3$.

3. Bogner-Fox-Schmit-Castro Finite Element with Single Curvature

The Bogner-Fox-Schmit-Castro (BFSC) finite element [19, 15] is a C1 contiguous confirming plate element obtained by taking tensor products of cubic Hermite splines. With 4 nodes per element and 10 degrees-of-freedom per node, the BFSC approximates the in-plane and out-of-plane displacements using 3^{rd}–order polynomials. In the present work, a single-curvature BFSC element (SC–BFSC) is proposed to combine the high-order interpolation of the BFSC with cylindrical shell kinematics, with the aim of achieving a computationally efficient and accurate representation of the variable stiffness shells under investigation. Figure 3 illustrates a SC–BFSC element and a global coordinate system xyz, where coordinate y is curvilinear following the circumferential perimeter, such that at $y = 2\pi r$ the path closes on itself. The nodal connectivity is also indicated, and the mesh is built to keep the element edges parallel to the x, y coordinates, such that $\ell_x = x_2 - x_1 = x_3 - x_4$, and $\ell_y = y_4 - y_1 = y_3 = y_2$. Figure 4 shows the mesh closing on itself at the intersection of elements e_{in} with elements e_{i1}. The natural coordinates are defined as $\xi = 2x/\ell_x - 1$ and $\eta = 2y/\ell_y - 1$, and with the proposed nodal connectivity, the values of ξ_i, η_i at each node, for all elements, are:

$$\begin{array}{ccc} Node & \xi_i & \eta_i \\ 1 & -1 & -1 \\ 2 & +1 & -1 \\ 3 & +1 & +1 \\ 4 & -1 & +1 \end{array} \tag{4}$$

The displacements along x, y, z are respectively u, v, w and can be approximated within each element as:

$$u_e, v_e, w_e = \textstyle\sum_{i=1}^{4} \boldsymbol{S}_i^{u,v,w} \boldsymbol{u_e}_i \tag{5}$$

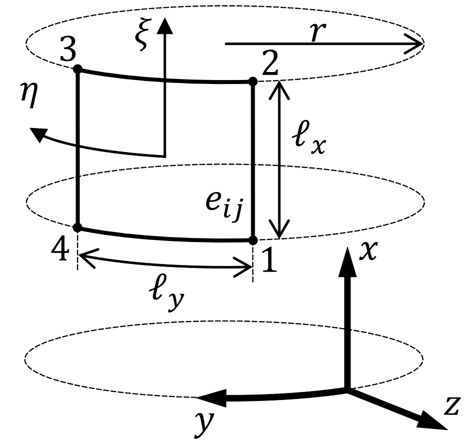

Figure 3: Single-curvature BFSC element and the global coordinate system xyz.

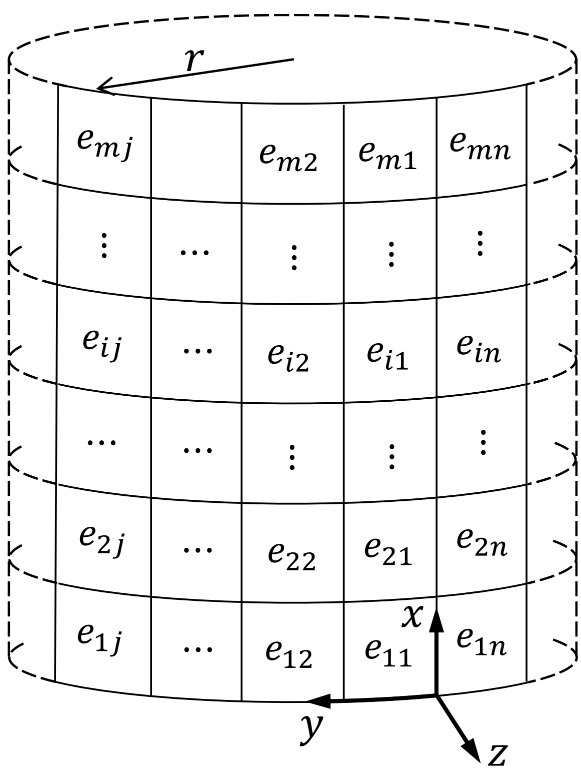

Figure 4: SC–BFSC mesh for the VAFW cylinders.

where $\boldsymbol{S}_i^{u,v,w}$ and $\boldsymbol{u}_{\boldsymbol{e}i}$ are the shape functions and the 10 degrees-of-freedom of the i^{th} node of the SC–BFSC element, being in the following order: u, $\partial u/\partial x$, $\partial u/\partial y$, v, $\partial v/\partial x$, $\partial v/\partial y$, w, $\partial w/\partial x$, $\partial w/\partial y$, $\partial^2 w/\partial x \partial y$. For the SC–BFSC element, the same shape functions of the plate BFSC element [15] can be used:

$$\begin{aligned} \boldsymbol{S}_i^u &= \begin{bmatrix} H_i & H_i^x & H_i^y & 0 & 0 & 0 & 0 & 0 & 0 & 0 \end{bmatrix} \\ \boldsymbol{S}_i^v &= \begin{bmatrix} 0 & 0 & 0 & H_i & H_i^x & H_i^y & 0 & 0 & 0 & 0 \end{bmatrix} \\ \boldsymbol{S}_i^w &= \begin{bmatrix} 0 & 0 & 0 & 0 & 0 & 0 & H_i & H_i^x & H_i^y & H_i^{xy} \end{bmatrix} \end{aligned} \tag{6}$$

with the cubic Hermite functions H_i, H_i^x, H_i^y, H_i^{xy} calculated using natural coordinates [20, 21, 22]:

$$\begin{aligned} H_i &= \tfrac{1}{16}(\xi+\xi_i)^2(\xi\xi_i-2)(\eta+\eta_i)^2(\eta\eta_i-2) \\ H_i^x &= -\tfrac{\ell_x}{32}\xi_i(\xi+\xi_i)^2(\xi\xi_i-1)(\eta+\eta_i)^2(\eta\eta_i-2) \\ H_i^y &= -\tfrac{\ell_y}{32}(\xi+\xi_i)^2(\xi\xi_i-2)\eta_i(\eta+\eta_i)^2(\eta\eta_i-1) \\ H_i^{xy} &= \tfrac{\ell_x\ell_y}{64}\xi_i(\xi+\xi_i)^2(\xi\xi_i-1)\eta_i(\eta+\eta_i)^2(\eta\eta_i-1) \end{aligned} \tag{7}$$

where ℓ_x, ℓ_y are respectively the finite element dimensions along x, y, as shown in Figure 3. Using the proposed nodal connectivity for the SC–BFSC element, the nodal degrees-of-freedom $\boldsymbol{u}_{\boldsymbol{e}i}$ and the respective shape functions $\boldsymbol{S}_i^{u,v,w}$ are concatenated as:

$$\begin{aligned} \boldsymbol{u}_{\boldsymbol{e}} &= \left\{\boldsymbol{u}_{\boldsymbol{e}1} \quad \boldsymbol{u}_{\boldsymbol{e}2} \quad \boldsymbol{u}_{\boldsymbol{e}3} \quad \boldsymbol{u}_{\boldsymbol{e}4}\right\}^\top \\ \boldsymbol{S}^u &= \begin{bmatrix} \boldsymbol{S}_1^u & \boldsymbol{S}_2^u & \boldsymbol{S}_3^u & \boldsymbol{S}_4^u \end{bmatrix} \\ \boldsymbol{S}^v &= \begin{bmatrix} \boldsymbol{S}_1^v & \boldsymbol{S}_2^v & \boldsymbol{S}_3^v & \boldsymbol{S}_4^v \end{bmatrix} \\ \boldsymbol{S}^w &= \begin{bmatrix} \boldsymbol{S}_1^w & \boldsymbol{S}_2^w & \boldsymbol{S}_3^w & \boldsymbol{S}_4^w \end{bmatrix} \end{aligned} \tag{8}$$

with $\boldsymbol{S}^u$, $\boldsymbol{S}^v$ and $\boldsymbol{S}^w$ being matrices of shape 1×40.

Assuming equivalent single-layer theory [23, 24], the total potential energy functional for one finite element ϕ_e can be expressed as:

$$\phi_e = \frac{1}{2} \int_{y=y_1}^{y_4} \int_{x=x_1}^{x_2} (\boldsymbol{N}\boldsymbol{\varepsilon} + \boldsymbol{M}\boldsymbol{\kappa})\, dx dy \tag{9}$$

where the membrane forces are $\boldsymbol{N} = \left\{N_{xx}, N_{yy}, N_{xy}\right\}^\top$ and the distributed moments are $\boldsymbol{M} = \left\{M_{xx}, M_{yy}, M_{xy}\right\}^\top$. The integration limits $x_1 \leq x \leq x_2$ and $y_1 \leq y \leq y_4$ define the domain of one finite element Ω_e. The membrane $\boldsymbol{\varepsilon}$ and rotational $\boldsymbol{\kappa}$ strains are assumed to follow von Kármán kinematics, also referred to in the literature as Donnell-type [25, 26] or Kirchhoff-Love non-linear equations, given by:

$$\begin{aligned} \boldsymbol{\varepsilon} &= \begin{Bmatrix} \varepsilon_{xx} \\ \varepsilon_{yy} \\ \gamma_{xy} \end{Bmatrix} = \begin{Bmatrix} u,_x + \frac{1}{2} w,_x^2 \\ v,_y + \frac{1}{r} w + \frac{1}{2} w,_y^2 \\ u,_y + v,_x + w,_x w,_y \end{Bmatrix} \\ \boldsymbol{\kappa} &= \begin{Bmatrix} \kappa_{xx} \\ \kappa_{yy} \\ \kappa_{xy} \end{Bmatrix} = \begin{Bmatrix} -w,_{xx} \\ -w,_{yy} \\ -2w,_{xy} \end{Bmatrix} \end{aligned} \tag{10}$$

with $(\cdot),_x = \partial(\cdot)/\partial x$ used as a compact notation for partial derivatives. At the bifurcation point, the following state of equilibrium exists, considering all n_e elements:

$$\delta\phi = \sum_{e=1}^{n_e} \delta\phi_e = \sum_{e=1}^{n_e} \int_{\Omega_e} \left(\boldsymbol{N}^\top \delta\boldsymbol{\varepsilon} + \boldsymbol{M}^\top \delta\boldsymbol{\kappa}\right) d\Omega_e = 0 \tag{11}$$

Expressing the displacements within one element in terms of nodal coordinates $\boldsymbol{u_e}$ as per Eq. 5, $\delta\boldsymbol{\epsilon}$ and $\delta\boldsymbol{\kappa}$ can be calculated as:

$$\delta\boldsymbol{\epsilon} = \begin{bmatrix} \boldsymbol{S}^u_{,x} + w_{,x}\boldsymbol{S}^w_{,x} \\ \boldsymbol{S}^v_{,y} + \frac{1}{r}\boldsymbol{S}^w + w_{,y}\boldsymbol{S}^w_{,y} \\ \boldsymbol{S}^u_{,y} + \boldsymbol{S}^v_{,x} + w_{,x}\boldsymbol{S}^w_{,y} + w_{,y}\boldsymbol{S}^w_{,x} \end{bmatrix} \delta\boldsymbol{u_e}$$
$$\delta\boldsymbol{\kappa} = \begin{bmatrix} -\boldsymbol{S}^w_{,xx} \\ -\boldsymbol{S}^w_{,yy} \\ -2\boldsymbol{S}^w_{,xy} \end{bmatrix} \delta\boldsymbol{u_e} \tag{12}$$

where the partial derivatives of $\boldsymbol{S}^{u,v,w}$ are directly calculated from the shape functions of Eq. 6 in terms of the natural coordinates ξ, η, using the following Jacobian relations:

$$\frac{\partial}{\partial x} = \frac{\ell_x}{2}\frac{\partial}{\partial \xi}$$
$$\frac{\partial}{\partial y} = \frac{\ell_y}{2}\frac{\partial}{\partial \eta} \tag{13}$$

The neutral equilibrium criterion also requires that $\delta^2\phi_e = 0$ [27], such that, from Eq. 11:

$$\delta^2\phi = \sum_{e=1}^{n_e} \delta^2\phi_e = \sum_{e=1}^{n_e} \left[\int_{\Omega_e} \left(\delta\boldsymbol{N}^\top \delta\boldsymbol{\epsilon} + \delta\boldsymbol{M}^\top \delta\boldsymbol{\kappa} +\right) d\Omega_e + \int_{\Omega_e} \left(\boldsymbol{N}^\top \delta^2\boldsymbol{\epsilon} + \boldsymbol{M}^\top \delta^2\boldsymbol{\kappa} +\right) d\Omega_e \right] = 0 \tag{14}$$

The first integral of Eq. 14 becomes the constitutive stiffness matrix of the element, calculated using the constitutive relations from classical laminated plate theory [24]:

$$\delta\boldsymbol{N} = \boldsymbol{A}\delta\boldsymbol{\epsilon} + \boldsymbol{B}\delta\boldsymbol{\kappa}$$
$$\delta\boldsymbol{M} = \boldsymbol{B}\delta\boldsymbol{\epsilon} + \boldsymbol{D}\delta\boldsymbol{\kappa}$$

Note that the geometric non-linearity appears in the constitutive stiffness matrix due to $w_{,x}, w_{,y}, w_{,xy}$ in Eq. 12. Therefore, the linear constitutive stiffness matrix of a finite element $\boldsymbol{K_e}$ is calculated by assuming $w_{,x}, w_{,y}, w_{,xy} = 0$, leading to a 40×40 matrix:

$$\begin{aligned}\boldsymbol{K_e} = \iint_{xy} & \begin{bmatrix} \boldsymbol{S}^u_{,x} \\ \boldsymbol{S}^v_{,y} + \frac{1}{r}\boldsymbol{S}^w \\ \boldsymbol{S}^u_{,y} + \boldsymbol{S}^v_{,x} \end{bmatrix}^\top \boldsymbol{A} \begin{bmatrix} \boldsymbol{S}^u_{,x} \\ \boldsymbol{S}^v_{,y} + \frac{1}{r}\boldsymbol{S}^w \\ \boldsymbol{S}^u_{,y} + \boldsymbol{S}^v_{,x} \end{bmatrix} \\ & + \begin{bmatrix} \boldsymbol{S}^u_{,x} \\ \boldsymbol{S}^v_{,y} + \frac{1}{r}\boldsymbol{S}^w \\ \boldsymbol{S}^u_{,y} + \boldsymbol{S}^v_{,x} \end{bmatrix}^\top \boldsymbol{B} \begin{bmatrix} -\boldsymbol{S}^w_{,xx} \\ -\boldsymbol{S}^w_{,yy} \\ -2\boldsymbol{S}^w_{,xy} \end{bmatrix} \\ & + \begin{bmatrix} -\boldsymbol{S}^w_{,xx} \\ -\boldsymbol{S}^w_{,yy} \\ -2\boldsymbol{S}^w_{,xy} \end{bmatrix}^\top \boldsymbol{B} \begin{bmatrix} \boldsymbol{S}^u_{,x} \\ \boldsymbol{S}^v_{,y} + \frac{1}{r}\boldsymbol{S}^w \\ \boldsymbol{S}^u_{,y} + \boldsymbol{S}^v_{,x} \end{bmatrix} \\ & + \begin{bmatrix} -\boldsymbol{S}^w_{,xx} \\ -\boldsymbol{S}^w_{,yy} \\ -2\boldsymbol{S}^w_{,xy} \end{bmatrix}^\top \boldsymbol{D} \begin{bmatrix} -\boldsymbol{S}^w_{,xx} \\ -\boldsymbol{S}^w_{,yy} \\ -2\boldsymbol{S}^w_{,xy} \end{bmatrix} dxdy \end{aligned} \tag{15}$$

The second integral of Eq. 14 becomes the geometric stiffness matrix of the finite element $\boldsymbol{K_{G0e}}$, capturing the geometrically nonlinear effects of a pre-buckling membrane stresses $\boldsymbol{N_0} = \left\{N_{0xx}, N_{0yy}, N_{0xy}\right\}^\top$ on the membrane stiffness. Noting that $\delta^2\boldsymbol{\kappa} = \boldsymbol{0}$ [15, 27], the equation for $\boldsymbol{K_{G0e}}$ becomes:

$$\boldsymbol{K_{G0e}} = \iint_{xy} \begin{bmatrix} \boldsymbol{S}^{w^\top}_{,x} N_{0xx}\boldsymbol{S}^w_{,x} \\ \boldsymbol{S}^{w^\top}_{,y} N_{0yy}\boldsymbol{S}^w_{,y} \\ \boldsymbol{S}^{w^\top}_{,y} N_{0xy}\boldsymbol{S}^w_{,x} + \boldsymbol{S}^{w^\top}_{,x} N_{0xy}\boldsymbol{S}^w_{,y} \end{bmatrix} dxdy \tag{16}$$

The contributions all n_e finite element are added to build the global constitutive stiffness matrix $\boldsymbol{K}$ and geometric stiffness matrix $\boldsymbol{K_{G0}}$ of the system:

$$\boldsymbol{K} = \sum_{e=1}^{n_e} \boldsymbol{K_e}$$
$$\boldsymbol{K_{G0}} = \sum_{e=1}^{n_e} \boldsymbol{K_{G0e}} \tag{17}$$

The pre-buckling stress field of one finite element $N_{0xx}, N_{0yy}, N_{0xy}$ is calculated from the corresponding nodal displacements $\boldsymbol{u_{0e}}$ as:

$$\boldsymbol{N_0} = \begin{Bmatrix} N_{0xx} \\ N_{0yy} \\ N_{0xy} \end{Bmatrix} = \boldsymbol{A} \begin{bmatrix} \boldsymbol{S}^u_{,x} \\ \boldsymbol{S}^v_{,y} + \frac{1}{r}\boldsymbol{S}^w \\ \boldsymbol{S}^u_{,y} + \boldsymbol{S}^v_{,x} \end{bmatrix} \boldsymbol{u_{0e}} \tag{18}$$

where $\boldsymbol{u_{0e}}$ is directly extracted from the full pre-buckling displacement vector $\boldsymbol{u_0}$ that is obtained from a static analysis, derived from the equilibrium of Eq. 11:

$$\boldsymbol{u_0} = \boldsymbol{K}^{-1}\boldsymbol{f_0} \tag{19}$$

with $\boldsymbol{f_0}$ represents any general pre-buckling force. When applied the neutral equilibrium criterion of Eq. 14 one assumes that at the bifurcation point there is a value of internal membrane stresses $\boldsymbol{N}$ based on the known pre-buckling stress $\boldsymbol{N_0}$ described by $\boldsymbol{N} = \lambda \boldsymbol{N_0}$ that leads to the condition $\delta^2\phi = 0$. Therefore, the problem consists of finding the value of λ that leads to:

$$\delta \boldsymbol{u}^{\top} \left(\boldsymbol{K} + \lambda \boldsymbol{K_{G0}}\right) \delta \boldsymbol{u} = 0 \tag{20}$$

which holds true for any variation $\delta\boldsymbol{u}$, such that the required condition for the equality of Eq. 20is:

$$\det\left(\boldsymbol{K} + \lambda \boldsymbol{K_{G0}}\right) = 0 \tag{21}$$

Equation 21 represents a linear buckling eigenvalue problem, where a characteristic polynomial in terms of λ can be obtained and solved. For a system with n unknown degrees-of-freedom, there are n eigenvalues that are roots of the characteristic polynomial. In practice, the eigenvalues and corresponding buckling modes are solved using generalized eigenvalue solvers that are able to efficiently extract only a desired number of eigenvalues and buckling modes, and in the present work the locally optimal block preconditioned conjugate gradient method [28] implemented in SciPy [29] is used.

The integration of $\boldsymbol{K_e}$ and $\boldsymbol{K_{G0e}}$ over the finite element domains are performed numerically using standard Gauss-quadrature with 4×4 integration points per element. The authors verified that this amount of integration points leads to a converged behavior. For each integration point, the local shell constitutive properties given by matrices $\boldsymbol{A}, \boldsymbol{B}, \boldsymbol{D}$ are calculated based on the winding angle distribution $\theta(x)$ of all angle–ply layers. While computing the constitutive matrices, the local thickness of each ply is consistently calculated according to Eq. 3. The elements of the constitutive matrices are functions of x, given by $A_{ij}(x)$, $B_{ij}(x)$, $D_{ij}(x)$, and are calculated with:

$$\begin{aligned} A_{ij}(x) &= \sum_{k=1}^{n} Q_{ij}(x)\left(z_k(x) - z_{k-1}(x)\right) \\ B_{ij}(x) &= \sum_{k=1}^{n} Q_{ij}(x)\frac{1}{2}\left(z_k(x)^2 - z_{k-1}(x)^2\right) \\ D_{ij}(x) &= \sum_{k=1}^{n} Q_{ij}(x)\frac{1}{3}\left(z_k(x)^3 - z_{k-1}(x)^3\right) \end{aligned} \tag{22}$$

where n is the number of plies; $Q_{ij}(x)$ is the ply stiffness rotated by the local winding angle $\theta(x)$ [24]; $z_k(x)$ defines the position of the outward face of the k^{th} ply. For a correct representation of the filament winding process, the inner face of the filament-wound cylinder must coincide with the mandrel radius. Therefore, the values of $z_k(x)$ are offset by a quantity $d(x)$ such that $z_{k-1} = 0$ for the first ply, as illustrated in Figure 5. The correct $d(x)$ value is half of the total thickness:

$$d(x) = \frac{1}{2}\sum_{k=1}^{n} h_k(x) \tag{23}$$

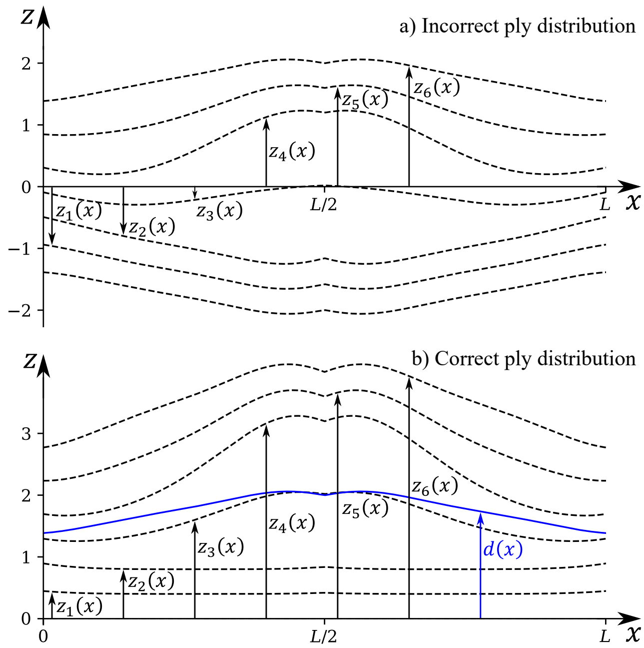

Figure 5: a) Incorrect ply distribution with a constant mid-surface at $z = 0$; and b) Correct ply distribution with a varying offset $d(x)$ applied to the mid-surface. The outward face position of all plies $z_k(x)$ for $k = 1, 2, \cdots, 6$ are shown.

where $h_k(x)$ is the local thickness of each ply as per Eq. 3. Appendix **??** presents a verification of the proposed finite element formulation compared with the multipurpose shell element S4R from Abaqus [30].

4. The metamodels

The metamodels are herein employed to decrease the computational costs of the design optimizations and to provide a better understanding of the design space, and three metamodeling approaches are considered, namely: Kriging, co-Kriging, and accelerated–Kriging. The metamodels are aimed at describing the hyper-surface of the buckling load and mass of filament–wound cylinders possessing different number of layers N_L and different winding angles $\pm\theta$.

Initially, Latin Hypercube Sampling (LHS) is used to generate the initial sample space with random variables. After this initial random sampling is generated, the first metamodel can be assembled in form of hyper-surfaces to describe the surface response of both design load and mass of the cylinders. The metamodel is then trained until all convergence requirements are satisfied, which depends on the number of variables and the degree of non–linearity of the response surface. For all metamodels two convergence criteria, $CC1$ and $CC2$, are adopted:
$CC1$: The predicted response error of both lower and upper boundaries must be less than a given threshold c. Then, $CC1$ is determined as:

$$Error^{i}_{lower} < c \quad \text{and} \quad Error^{i}_{upper} < c \tag{24}$$

where $Error^{i}_{lower}$ and $Error^{i}_{upper}$ are the errors of the lower and upper boundaries in the i^{th} training process, respectively. The $Error$ is then defined as:

$$Error = \frac{\left|\hat{y}(\theta_c) - y(\theta_c)\right|}{y(\theta_c)} \tag{25}$$

where $\hat{y}(\theta_c)$ and $y(\theta_c)$ are the predicted response and the true response of the candidate sample θ_c in design region, respectively. Three thresholds c are set to $5\%, 3\%, 1\%$ and applied to find the buckling load and mass limits of all cylinders. Each threshold generates particular limits and they will be useful to select the threshold with the widest range in terms of both buckling load and mass in order to enlarge the design space, therefore, increasing the chances of reaching higher improvements.

CC2: The error for both lower and upper boundaries in two consecutive cycles should be less than the given threshold c, which is determined as:

$$\left\{\begin{array}{l}\text{Error}^i_{lower} < c \text{ and Error }^i_{upper} < c \\ \text{Error}^{i-1}_{lower} < c \text{ and Error}^{i-1}_{upper} < c\end{array}\right. \tag{26}$$

The training process stops if the two converge criteria are met. Then, the lower and upper boundaries of the buckling load and mass can be estimated as:

$$\left\{\begin{array}{l}B_{lower} = \min\left[p^{i-1}_{lower}, p^i_{lower}\right] \\ B_{upper} = \max\left[p^{i-1}_{upper}, p^i_{upper}\right]\end{array}\right. \tag{27}$$

In the following sub-sections, each metamodel is explained in detail.

4.1. Kriging

For the Kriging metamodel, the spatial association between the design variables and the responses is expressed as:

$$\hat{f}(\boldsymbol{x}) = \boldsymbol{h}(\boldsymbol{x})^T\boldsymbol{v} + \Delta(\boldsymbol{x}) \tag{28}$$

where $\hat{x}$ is the predicted response, $\left[h_1(\boldsymbol{x}), h_2(\boldsymbol{x}), \dots, h_n(\boldsymbol{x})\right]$ is a vector of regression function which is also known as the trend of the prediction based on available samples, $\left[v_1, v_2, \dots, v_n\right]$ is a vector of coefficients, and $\Delta(\boldsymbol{x})$ is a Gaussian process with zero mean and covariance $cov\left(\Delta\left(\boldsymbol{x}_i\right), \Delta\left(\boldsymbol{x}_j\right)\right)$.

The initial random sample space, which is generated through LHS, has a population size of ten times the number of design variables, as recommended by Forrester et al. [31]. After that, the true responses for buckling load and mass are calculated by the FE analysis (FEA) described in section 3. Then, the initial samples and responses are used to construct the initial Kriging metamodel [32]. A training process follows to locate and add new samples into the metamodel, with new training samples selected as the sample with maximum mean square error (MSE) of the prediction, defined as follows:

Table 1
Detailed procedure of the Kriging metamodel for an arbitrary cylinder with one $\pm\theta(x)$ layer.

Step	*Procedure*
1:	Design variables $[\theta_1, \theta_2, \theta_3]$ and $N = 3$, set $i = 1$
2:	Generate 10 initial samples ($\chi_{initial}$)
3:	Obtain the buckling load of initial samples
4:	Construct initial metamodel with DACE tool, M^K_{i-1}
5:	Train the metamodel
5.1:	Locate sample χ_i with maximum MSE
5.2:	Obtain the buckling load λ_i of χ_i
5.3:	Add χ_i and λ_i to model M^K_{i-1}
6:	Estimate the boundaries λ^i_{lower} and λ^i_{upper}
6.1:	If $CC1$ and $CC2$ are satisfied, go to Step 7
6.2:	Else, $i = i + 1$, go back to Step 5
7:	Obtain the boundaries with Eq. 27.

$$\text{MSE} = \frac{1}{n}\sum_{k=1}^{n}\left[(\hat{y}(\theta_k) - y(\theta_k))^2\right] \tag{29}$$

where $\hat{y}(\theta_k)$ and $y(\theta_k)$ are the prediction and true responses for the sample θ_k, respectively.

The training process is repeated until the convergence criteria (Eqs. 24, 26) are satisfied. In addition, the lower and upper boundaries of the response in the design region are determined by Eq. 27. A detailed description of the procedure is given in Table 1.

4.2. Co-Kriging

The second metamodel exploited here uses the co-Kriging principles, which is also employed to predict the buckling load and mass of the VAFW-P cylinders. The co-Kriging is, essentially, an the extension of the Kriging approach, commonly used to approximate a surface or hyper-surface of a system response that is computationally expensive to estimate while the response of the system is dependent on a set of trained data, becoming computationally inexpensive [33].

In co-Kriging, the metamodel is built with two sets of data, one set named expensive data (θ_e, y_e) that are more computationally costly, while the other set is called cheap data (θ_c, y_c). These two sets of data are independent of each other. The response y_e at θ_e is supposed to be more accurate than the cheap data y_c at θ_c. The required total data are combined as:

$$\boldsymbol{\theta_r} = \begin{pmatrix}\boldsymbol{\theta}_e \\ \boldsymbol{\theta}_c\end{pmatrix} = \left(\theta_e^{(1)}, \dots, \theta_e^{(n_e)}, \theta_c^{(1)}, \dots, \theta_c^{(n_c)}\right)^{\mathrm{T}} \tag{30}$$

where θ_r are the required samples of random variables; θ_e and θ_c are random samples from expensive and cheap data, respectively; n_e and n_c are the number of expensive and cheap data, respectively. In this work, the number of data n_e and n_c are defined as

$$n_e = 2 \times n; n_c = 10 \times n \tag{31}$$

where n is the number of random variables.

The responses corresponding to the random samples θ_r are shown in Eq. 32, and the combined data $(\boldsymbol{\theta_r}, \boldsymbol{y_r})$ are the required data to build the co-Kriging metamodel.

$$\boldsymbol{y_r} = \left(y_e \left(\theta_e^{(1)} \right), \dots, y_e \left(\theta_e^{(n_e)} \right), y_c \left(\theta_c^{(1)} \right), \dots, y_c \left(\theta_c^{(n_c)} \right) \right)^{\mathrm{T}} \tag{32}$$

Similarly to Kriging approach, co-Kriging realizes the response surface with the required data through Eqs. 30,32. With the cheap data (θ_c, y_c), the response of the cheap function is described as a Gaussian process $f_c(\boldsymbol{\theta})$ in the total sample space [32]. Then, the expensive response surface is defined as:

$$f_e(\boldsymbol{\theta}) = \rho f_c(\boldsymbol{\theta}) + f_d(\boldsymbol{\theta}) \tag{33}$$

where $f_e(\boldsymbol{\theta})$ is the prediction at $\boldsymbol{\theta}$, ρ is a scaling factor estimated by the data, and $f_d(\boldsymbol{\theta})$ is the difference between expensive and cheap responses.

The initial independent cheap χ_c and expensive χ_e samples of random variables are generated via LHS. The buckling loads λ_c of samples χ_c are obtained from the Kriging metamodel (Section4.1), and the buckling loads λ_e of samples χ_e are calculated by FEA. Then, the metamodel can be built with the initial required data: (χ_c, λ_c) and (χ_e, λ_e).

Now that the core of the co-Kriging metamodel is set, the training process can take place. In each iteration of the training, three new training samples are added to the current metamodel. During the i^{th} iteration ($i = 1, 2, ..., n$), the first training sample is the point at where the MSE is the highest in the whole design region, expressed as χ_i. The buckling load λ_i of the sample χ_i is estimated FEA. The second and third new training samples are determined as the samples at the current lower and upper boundaries of the i^{th} metamodel, which are expressed as (χ_i^L, λ_i^L) and (χ_i^U, λ_i^U), respectively. Once the new training samples are available, they are added to the i^{th} metamodel to improve the accuracy of the predictions. The first sample (χ_i, λ_i) in the i^{th} iteration is added to the expensive data since it is likely to be accurate. The expensive data in the $(i + 1)^{th}$ iteration is then updated as:

$$\left(\boldsymbol{\chi}_e^{i+1}, \boldsymbol{\lambda}_e^{i+1} \right) = \left(\left[\boldsymbol{\chi}_e^i, \chi_i \right], \left[\boldsymbol{\lambda}_e^i, \lambda_i \right] \right) \tag{34}$$

where $\left(\boldsymbol{\chi}_e^{i+1}, \boldsymbol{\lambda}_e^{i+1} \right)$ is the expensive data in the $(i + 1)^{th}$ iteration, and $\left(\boldsymbol{\chi}_e^i, \boldsymbol{\lambda}_e^i \right)$ is the expensive data in the i^{th} iteration.

Then, the other new training samples (χ_i^L, λ_i^L) and (χ_i^U, λ_i^U) are added to the cheap data. The cheap data in the $(i + 1)^{th}$ iteration is then updated as:

$$\left(\boldsymbol{\chi}_c^{i+1}, \boldsymbol{\lambda}_c^{i+1} \right) = \left(\left[\boldsymbol{\chi}_c^i, \chi_i^L, \chi_i^U \right], \left[\boldsymbol{\lambda}_C^i, \lambda_i^L, \lambda_i^U \right] \right) \tag{35}$$

Table 2
Detailed procedure of the co-Kriging metamodel for an arbitrary cylinder with one $\pm\theta(x)$ layer.

Step	*Procedure*
1:	Design variables $[\theta_1, \theta_2, \theta_3]$ and $N = 3$, set $i = 1$
2:	Generate 10 initial samples $(\chi_{initial})$
3:	Obtain the buckling load of initial samples
4:	Construct initial co-Kriging metamodel M_{i-1}^K
5:	Train the metamodel
5.1:	Locate sample χ_i with maximum MSE
5.2:	Locate sample χ_i^L and χ_i^U of the boundaries of M_{i-1}^C
5.3:	Obtain buckling loads λ_i, λ_i^L, λ_i^U of χ_i, χ_i^L, χ_i^U
5.4:	Add $[\chi_i, \lambda_i]$ to samples $[\chi_e, \lambda_e]$
5.5:	Add $[\chi_i^L, \lambda_i^L]$ and $[\chi_i^U, \lambda_i^U]$ to samples $[\chi_c, \lambda_c]$
5.6:	Obtain new model M_i^C
6:	Estimate the boundaries λ_{lower}^i and λ_{upper}^i of M_i^C
6.1:	If $CC1$ and $CC2$ are satisfied, go to Step 7
6.2:	Else, $i = i + 1$, go back to Step 5
7:	Obtain the boundaries with Eq. 27.

where $\left(\boldsymbol{\chi}_c^{i+1}, \boldsymbol{\lambda}_c^{i+1} \right)$ is the cheap data in the $(i + 1)^{th}$ iteration, and $\left(\boldsymbol{\chi}_c^i, \boldsymbol{\lambda}_c^i \right)$ is the cheap data in the $(i)^{th}$ iteration.

After the updated expensive and cheap data are available, the metamodel is then trained. The lower and upper boundaries $(\chi_{i+1}^L, \lambda_{i+1}^L)$ and $(\chi_{i+1}^U, \lambda_{i+1}^U)$ are estimated by the extreme value optimization algorithm. In this work, the Particle Swarm Optimization (PSO) algorithm is employed, which is explained in section 5. The training process evolves until both convergence criteria $CC1$ and $CC2$ are met. Finally, the lower and upper boundaries of the buckling load in the design space can be calculated by Eq. 27.

Table 2 summarizes the procedure to find the buckling load boundaries through co-Kriging approach, in which the VAFW-P design with one $\pm\theta(x)$ layer is taken as a mere example.

4.3. Accelerated Kriging

During the approximation of the hyper-surface for the buckling load and mass carried out through both Kriging and Co-Kriging metamodels, considerable efficiency and accuracy have been reached. However, their performance is significantly affected by the number of variables in the system and the level of non-linearity of the system response, especially with regards to the number of iterations needed to train the metamodels for the required convergence criteria. With the aim to overcome this issue, an accelerated Kriging metamodel is introduced, which has been proven to be computationally efficient, accurate and improved in terms of convergence to optimize the buckling load of VAFW-P cylinders [13]. With an increasing number of variables or an increase in the non-linearity of the response, there is a large possibility that the sample with largest MSE is located at a design space region that is too far away from the optimum region, thus reflecting in a slow convergence of the conventional Kriging and Co-Kriging methods during the training phase. The proposed accelerated Kriging metamodel is an extension of the conventional Kriging approach, whereby a moving search window, or hyper-cube, is used during the training phase, allowing the addition of a new sample near the current optimum, speeding up the convergence whereas keeping the robustness of the original method.

The training process starts with initial random samples generated via LHS, in which the number of samples is the same used in the conventional Kriging metamodeling explained in Section 4.1. The responses of these samples are estimated by FEA. After the initial samples and the responses are computed, the initial metamodel is created using the DACE toolbox in Matlab [32]. Next, for each training iteration two points are added, being the first training point the one with largest MSE, similarly to the other two Kriging metamodels previously described. The second training point of the accelerated Kriging approach is added based on the largest MSE within an adaptive moving search window centered at the current optimum. The adaptive moving search window is defined as:

$$\left[\theta_{i+1}^{L}, \theta_{i+1}^{U}\right] = \left[\theta_{opt}^{i} - 0.5W, \theta_{opt}^{i} + 0.5W\right] \tag{36}$$

where θ_{i+1}^{L} and θ_{i+1}^{U} are the lower and upper boundaries of the $(i+1)^{th}$ adaptive window, respectively; The θ_{opt}^{i} is the i^{th} optimal design in the i^{th} iteration of the training procedure; W is the range of the window, which is determined as:

$$W = q \cdot \left(\theta^{L} + \theta^{U}\right) \tag{37}$$

where θ^{L} and θ^{U} are respectively the lower and upper boundaries of the design space, while q is a scale factor, which ranges from 0 to 1.

Considering that the center of the window is the previous optimal result (Eq. 36), the search window adapts itself by moving during the training iterations. In this work, a constant window width of $q = 0.25$ is used. The lower and upper boundaries of the i^{th} adaptive moving window is replaced by the corresponding lower and upper boundaries of the design space if the i^{th} window moves out of the design space, as follows:

$$\begin{cases} \theta_{i}^{L} = \theta^{L}, \text{ if } \theta_{i}^{L} < \theta^{L} \\ \theta_{i}^{U} = \theta^{U}, \text{ if } \theta_{i}^{U} > \theta^{U} \end{cases} \tag{38}$$

With the first and second training samples determined, the corresponding responses are estimated by FEA. The new samples and responses are then added to the metamodel. The iterations are repeated until the convergence criteria $CC1$ and $CC2$ are met. Table 3 describes a summary of the proposed approach for a VAFW-P cylinder with one ± layer.

4.4. Design space analysis for buckling loads

After the convergence criteria ($CC1$, $CC2$) and thresholds (5%, 3%, 1%) are met for all three Kriging-based metamodels, the lower and upper boundaries for the buckling loads are estimated. Table 4 shows the obtained boundaries and the required number of samples N_s used in the training process for the VAFW-P design with one layer ($N_L = 1$). It is observed that the accelerated-Kriging metamodel provides the widest ranges in terms of buckling loads for all thresholds applied. Focusing specifically on the threshold $c = 1\%$, which provides wider boundaries, the more the number of layers, the higher the number of new samples (N_S) required to the training process, as shown in Table 5. Therefore, given the wider boundaries mapped by the accelerated-Kriging metamodel, which is an indicative of a higher accuracy, its results are used to estimate the buckling loads and mass for $N_L = 2, 3, 4$.

Table 6 summarizes the estimated lower and upper boundaries of buckling load for the VAFW-P cylinders with $N_L = 1, 2, 3, 4$, obtained with the accelerated-Kriging metamodel. Note that this is a key task accomplished by the metamodel, resulting in a better understanding of the design space.

Table 3
Detailed procedure of the accelerated-Kriging metamodel for an arbitrary cylinder with one $\pm\theta(x)$ layer.

Step	*Procedure*
1:	Design variables $[\theta_1, \theta_2, \theta_3]$ and $N = 3$, set $i = 1$
2:	Generate 10 initial samples ($\chi_{initial}$)
3:	Obtain buckling load of initial samples
4:	Construct initial Kriging metamodel M_{i-1}^{A}
5:	Train the metamodel
5.1:	Locate sample χ_i with maximum MSE
5.2:	Locate sample χ_i^W with the adaptive moving window
5.3:	Obtain buckling loads λ_i, λ_i^W of χ_i, χ_i^W
5.4:	Add $[\chi_i, \lambda_i]$ and $[\chi_i^w, \lambda_i^w]$ to the training samples
5.5:	Obtain new model M_i^A
6:	Estimate the boundaries λ_{lower}^{i} and λ_{upper}^{i} of M_i^A
6.1:	If $CC1$ and $CC2$ are satisfied, go to Step 7
6.2:	Else, $i = i + 1$, go back to Step 5
7:	Obtain the boundaries with Eq. 27.

4.5. Mass metamodeling

The mass of the cylinders is calculated as:

$$m = \iint_{xz} \rho h(x, z) r dx dz \tag{39}$$

where m is the mass, ρ is the density of the carbon/epoxy composite material ($1600\,kg/m^3$), x is the circumferential coordinate, z is the longitudinal coordinate, r is the radius of the cylinder, and $h(x, z)$ is the thickness.

To calculate the mass for the cylinders with several layers, a simple function to sum of the mass of every layer is considered:

$$M(\theta, N_L) = \sum_{i=1}^{N_L} m_i(\theta_i), N_L = 1, 2, 3, 4 \tag{40}$$

Table 4
Converged lower and upper boundaries of buckling loads for VAFW-P with $N_L = 1$ for the three Kriging–based metamodels.

	Kriging			Co-Kriging			Accelerated-Kriging		
	$c = 5\%$	$c = 3\%$	$c = 1\%$	$c = 5\%$	$c = 3\%$	$c = 1\%$	$c = 5\%$	$c = 3\%$	$c = 1\%$
$\lambda_L^2\ [N]$	34,534	34,534	34,304	33,955	33,955	33,615	34,842	34,842	33,729
$\lambda_U^2\ [N]$	65,914	65,914	66,160	66,733	66,733	67,901	67,946	67,946	68,768
N_s	2	2	4	6	6	21	6	6	30

Table 5
Number of required samples to train all three Kriging–based metamodels for a threshold of $c = 1\%$.

Metamodel	Number of layers (N_L).			
	1	2	3	4
N_S: Kriging	2	25	85	102
N_S: Co-Kriging	7	51	63	126
N_S: Accelerated-Kriging	21	81	108	183

Table 6
Converged boundaries of buckling loads for the VAFW-P design using the accelerated-Kriging metamodel.

Boundaries	Number of layers (N_L)			
	1	2	3	4
$\lambda_L^{N_L}\ [N]$	33,729	146,190	329,563	694,931
$\lambda_U^{N_L}\ [N]$	68,768	1,852,980	2,909,814	3,496,871

Table 7
Lower and upper mass limits for all cylinder designs.

Boundaries	Number of layers (N_L)			
	1	2	3	4
$M_L^{N_L}\ [kg]$	0.3644	0.7288	1.0932	1.4576
$M_U^{N_L}\ [kg]$	6.9796	13.9592	20.9388	27.9184

where m_i is the mass of the i^{th} layer, and θ_i is the winding angles in the i^{th} layer. Once the boundaries of the mass for two layers is computed, the boundaries for the other cylinders can be calculated by Eq. 40. Then, the lower and upper limits for all cylinders are listed in in Table 7.

Figure 6 illustrates the hyper–surfaces of both buckling loads and mass for the cylinders trained with the accelerated–Kriging metamodel using Monte Carlo sampling (MCS). Considering that there are three design variables, one of them is kept constant at 45° to allow a convenient graphic representation. Then, after both metamodels for buckling loads and mass are trained, the optimization follows, as detailed next.

Figure 7 illustrates the outcome of the trained metamodels by plotting the buckling load λ versus the mass for several sample sizes by using MCS approach. Throughout the optimization procedure the samples are dynamically generated, as explained in section 5. From Figure 7 there is a clear trend of higher buckling loads for higher mass values, and it can be observed a complex mass distribution created by the coupled steering-thickness coupling of the VAFW-P cylinder design. From the sampling with 2000 samples of Figure 7(f), the minimum and maximum intervals of mass and buckling loads were identified for $N_L = 1, 2, 3, 4$, as shown in Figure 8. Note that for design loads below $\approx 69\ kN$ only designs with $N_L = 1$ should be considered, whereas for a design load of $\approx 700\ kN$, all designs with $N_L = 2, 3, 4$ might

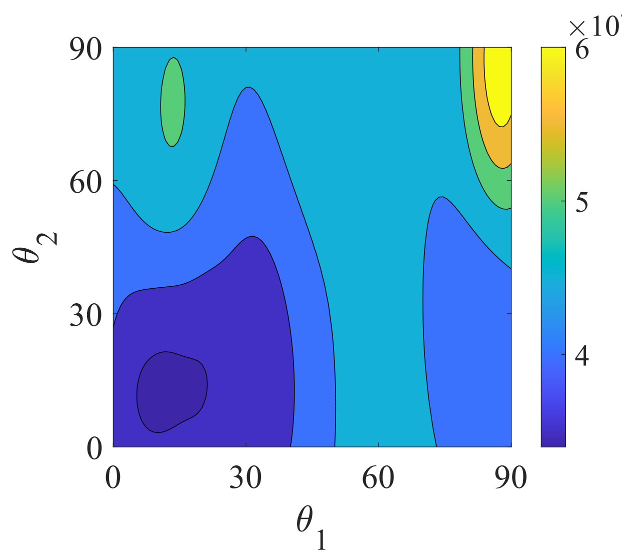

(a) Buckling load surface, kN

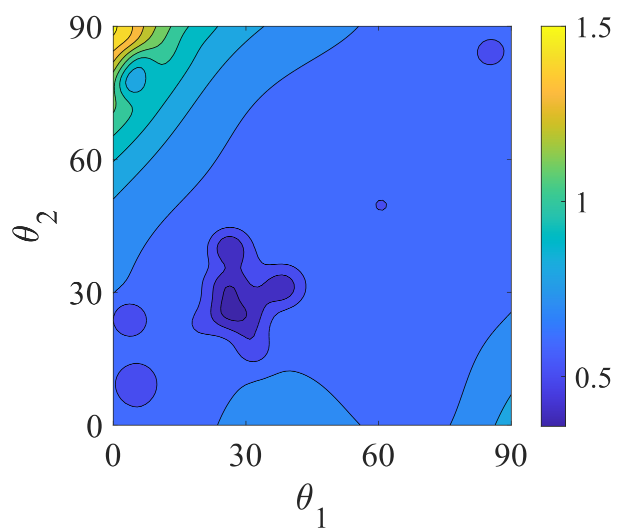

(b) Mass surface, kg

Figure 6: Contour plots using the accelerated-Kriging metamodel with $N_L = 1$ (one $\pm$ layer). For plotting purposes, assuming $\theta_3 = 45°$.

lead to optimum solutions and should therefore be considered by the optimization algorithms. Figure 8 also shows a gap in the design space between $\approx 69\,kN$ and $\approx 146\,kN$.

5. The optimization

5.1. Particle Swarm Optimization (PSO)

The PSO is a powerful meta-heuristic technique inspired on the swarm behavior of flocks of birds and shoals of fishes, and developed by Kennedy and Eberhart in 1995 [34]. The method is also related to evolutionary computation and it has some ties to genetic algorithm (GA). The key advantages of PSO are that it needs only primitive mathematical operations and it is computationally cheap in terms of memory and speed requirements.

In PSO, a swarm with particles P is placed in the design search space. Each i^{th} particle in the swarm has a position vector $X_i^t = \left(x_{i1}, x_{i2}, x_{i3}, \dots, x_{in}\right)^T$ and velocity vector $V_i^t = \left(v_{i1}, v_{i2}, v_{i3}, \dots, v_{in}\right)^T$ at iteration t. Each particle is updated according to the dimension j, as per Eq. 41. Every particle is a potential candidate solution and they move continuously around the design space until the optimization meets the convergence criteria. The new particle locations are updated at every iteration towards finding the global optimum. The velocity of the particles can be defined as:

$$V_{ij}^{t+1} = wV_{ij}^t + c_1 r_1^t \left(pbest_{ij} - X_{ij}^t\right) + c_2 r_2^t \left(gbest_j - X_{ij}^t\right) \tag{41}$$

whereas the new position is calculated as:

$$X_{ij}^{t+1} = X_{ij}^t + V_{ij}^{t+1} \tag{42}$$

in which V_i^d X_i^d are the velocity and position of the i^{th} particle, respectively; c_1 and c_2 are acceleration constants; r_1^t and r_2^2 represent two random numbers distributed in the range (0,1); $pbest$ and $gbest$ are the best position so far of the i^{th} particle and the best global position, respectively; w is the inertia weight, which keeps a balance between local and global searches.

Once the buckling load and mass hyper-surfaces are constructed (Section 4), the PSO procedure takes place, whose optimization problem is formulated as:

$$\begin{aligned}
&Find : \theta_{i,L}^{VP}, N_L; \text{for } i = 1, 2, 3; \text{ and: } L = 1, \cdots, N_L \\
&Minimize : M(\theta_{i,L}^{VP}, N_L) \\
&Subject\ to : \lambda(\theta_{i,L}^{VP}, N_L) > \lambda_d \\
&\theta^L \le \theta_{i,L}^{VP} \le \theta^U; \text{for } \theta^L = 3.3^\circ \text{ and } \theta^L = 87.7^\circ
\end{aligned} \tag{43}$$

where $\theta_{i,L}^{VP}$ are the angle at the control points for each layer L; θ^L and θ^U are the lower and upper boundaries for the filament angle; and N_L the total number of layers to be determined. Note that, from the sampling previously performed and shown in Figure 7, it is possible to determine all possible values of N_L for a given design load, as illustrated in Figure 8, and for the region with a gap in the design space from $\approx 69\,kN$ to $\approx 146\,kN$ it was assumed $N_L = 2$.

Table 8
Parameters used in the PSO–MM optimization.

Parameter	Value
Number of variables (N_L)	1, 2, 3, 4
Minimum inertia weight (W_{min})	0.4
Maximum inertia weight (W_{max})	0.9
Acceleration factors ($c_1 = c_2$)	2
Population size	20
Maximum iterations	100
Number of swarms	1

The parameters utilized in the PSO–metamodeling (PSO–MM) optimization framework are presented in Table 8.

In each optimization run shown in Eq. 43, the particle with minimum mass is searched for 5 desired buckling loads: 50 kN, 100 kN, 200 kN, 500 kN, and 1000 kN. Then, for each maximum desired load, the optimization finds both optimum angles θ_{opt} and number of layers N.

The overall mass minimization procedure to meet desired buckling loads BL_d can be summarized as follows:

S1: For any given desired buckling load, the number of layers is determined with the boundary analysis of the buckling load shown in Table 6. The candidate number of layers N is determined as

$$N = [2i, \dots, 2j] \tag{44}$$

in which,

$$i, j \in [1, \dots, 4], \text{ where } i \le j \tag{45}$$

S2: Set $n = i$;

S3: The number of layers is then $N = 2n$ and the number of design variables (θ_n^{opt}) is $3n$.
The optimization flowchart is illustrated in Figure 9, starting by calling both buckling load metamodels in each iteration. Then, the PSO algorithm finds the minimum mass, M_n^{min}, within the buckling load boundaries, as detailed in the following steps:

S4: If $n < j$, $n = n + 1$, go back to Step3. Else, go to S5;

S5: Obtain all the candidate optimal designs and corresponding masses:

$$\left[\theta_\tau^{\text{opt}}, M_\tau^{\text{min}}\right], \tau = [1, \dots, n] \tag{46}$$

S6: Select the sample with the minimum mass of all candidates using Eq. 46 as the optimum for a given design load BL_d. Then, the final output, θ_{final}^{opt}, is generated;

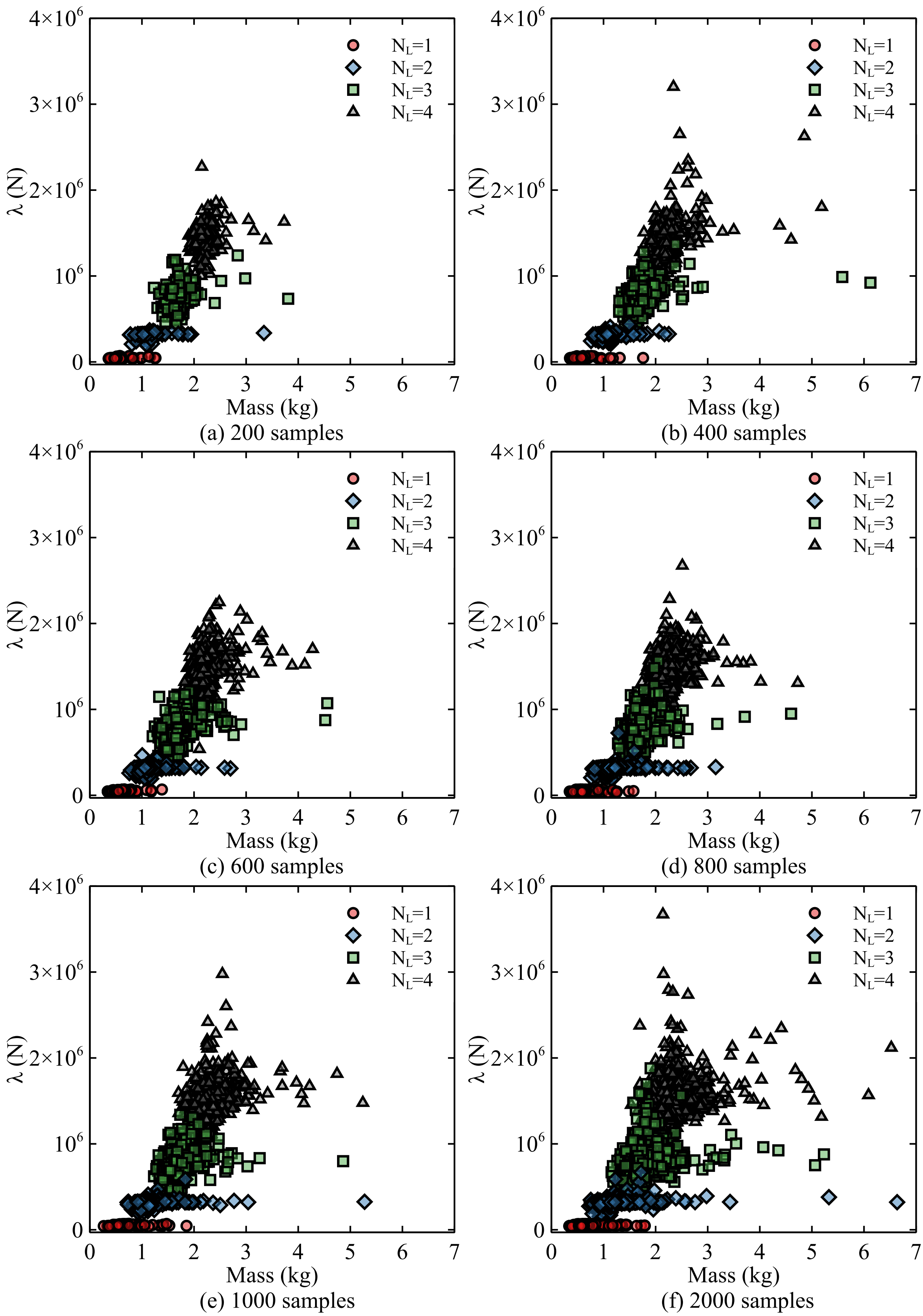

Figure 7: Design space illustrated using the buckling load λ versus mass for different samples generated using the developed metamodels.

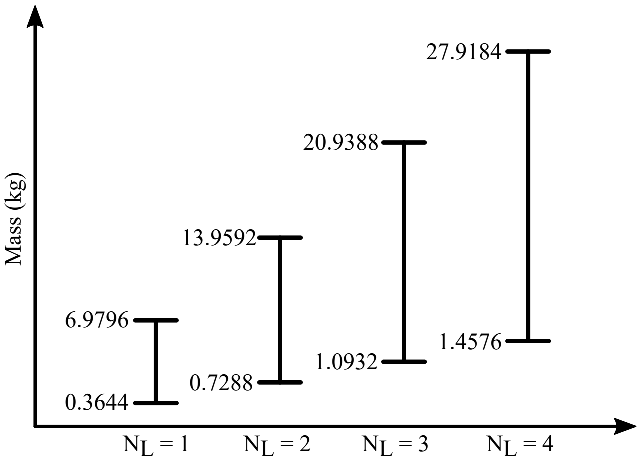

(a) Mass boundaries

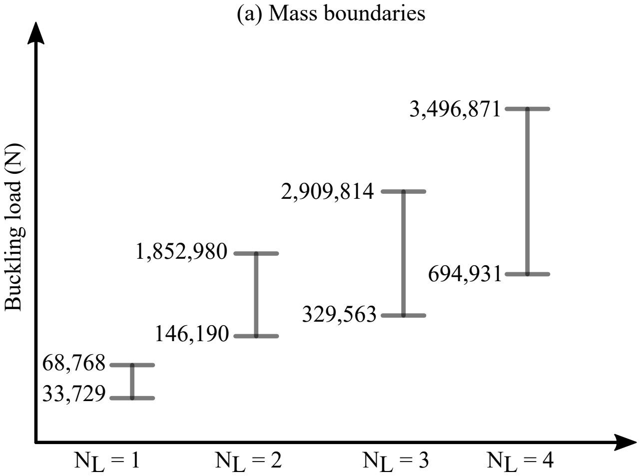

(b) Buckling load boundaries

Figure 8: Mass and buckling load boundaries defined by the metamodels using 5000 samples.

5.2. Optimization verification: genetic algorithm (GA)

Optimizations using a genetic algorithm (GA) along with the developed SC–BFSC FE model are used to verify the optimization results from the PSO–MM framework. The GA is implemented in OpenMDAO, an open–source optimization framework [35]. It is worth mentioning that the number of layers allowed are the same as in the PSO–MM optimizations, that is, $N_L = 1, N_L = 2, N_L = 3, N_L = 4$. The parameters utilized in the optimizations are presented in Table 9. The objective function is similar to Eq. 43, whereby the function is changed in accordance with the GA problem definition as shown in Eq. 47:

$$\begin{aligned}
&\text{Find}: \theta, N_L \\
&\text{Minimize}: M(\theta, N_L) \times PF \\
&\text{Penalty Function}(PF): \begin{cases} 1 & \text{if } \lambda \geq \lambda_d \\ (1+\lambda_d/\lambda)^2 & \text{if } \lambda < \lambda_d \end{cases} \\
&\text{Design Space:} \quad \epsilon \quad [0, 90]
\end{aligned} \tag{47}$$

Table 9
Parameters used in the GA optimization.

Parameter	Value
Bit size (B_s)	6
Maximum generations	100
Population size	$8 \times B_s$
Mutation rate	0.02

where M is the mass calculated according to Eq. 40; λ is the buckling load of the individual; and λ_d is the design buckling load.

5.3. Optimization results

The objective function of the optimizations is to minimize the cylinder mass subject to the following design loads: 50 kN, 100 kN, 200 kN, 500 kN, and 1000 kN. The PSO-MM results consist of optimum designs obtained per design load, where different optima are obtained for different number of $\pm\theta$ layers in the filament winding process. The GA results consist of only one optimum design per design load. The results are given in Table 10.

From Table 10, the following characteristics of the optimum designs, and the differences between the PSO-MM and GA results are identified:

- ***50 kN***: this design load is covered by candidates with $N_L = 1$, as illustrated in Figure 8. The GA results is slightly heavier than the PSO-MM result;
- ***100 kN***: from Figure 8 there is no design covering this design load, and this region represents part of a gap in the design space from $\approx 69\ kN$ to $\approx 146\ kN$. The PSO-MM optimization found a candidate cylinder with $N_L = 2$, with a buckling load of 165.33 kN, expectedly higher than the 100 kN design load, due to the gap in the design space previously identified. Interestingly, the GA result confirmed the identified gap by finding an optimum solution outside the gap region, with a buckling load of 288.15 kN, and a comparable mass with respect to the optimum design obtained by the PSO-MM;
- ***200 kN***: the only candidate for this design load level are those with $N_L = 2$. The combination of angles leads to shell with a mass of 0.7309 kg and buckling load of 207.61 kN. The GA, nevertheless, does not find an optimum with buckling load around the desired one. However, the optimum found by GA has a similar mass with a substantially higher buckling load of 242.83 kN;
- ***500 kN***: as per Figure 8 this design load is covered by cylinders with $N_L = 2$ and $N_L = 3$, and the PSO-MM optima have respective masses of 1.2715 kg and 1.0951 kg; with buckling loads of 498.29 kN and 504.28 kN. The GA finds a unique optimum candidate with $N_L = 3$, with optimum mass comparable to the PSO-MM result, and a higher buckling load of 659.80 kN;

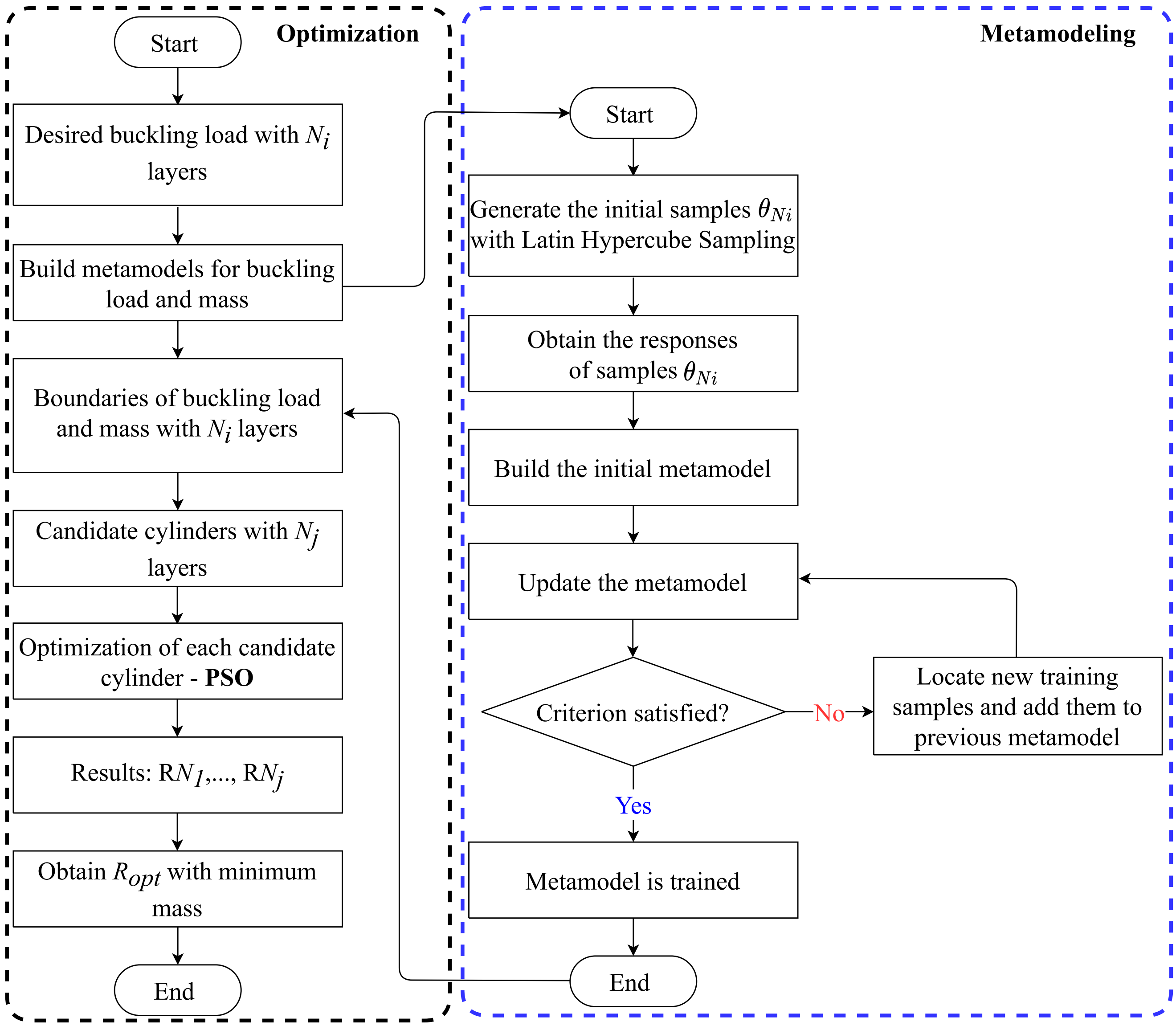

Figure 9: Flowchart of the proposed PSO–MM framework.

- ***1000 kN***: three candidates are found by the PSO–MM to respect this desired load, with 2, 3, and 4 $\pm\theta$ layers. They have masses between 1.46 and 1.61 kg with buckling loads within a range of 1021.5 and 1092.2 kN, respectively. The GA finds only one candidate with 4 $\pm\theta$ layers, which has similar mass to the candidate with 4 layers found by PSO–MM framework, with 1.46 kg but with a higher buckling load of 1301.7 kN.

The GA optima reached considerably higher buckling loads without resulting in additional mass for the design loads of 200 kN, 500 kN and 1000 kN, shown in Table 10. This is not due to the objective function of Eq. 47 utilized in the GA optimizations, where the buckling load λ only participates in the penalty function when $\lambda < \lambda_d$, with λ_d being the design load.

6. Discussion

The PSO-MM optimum designs listed in Table 10 are illustrated in Figures 10 – 17. The illustrated layers k_i are stacked in an increasing z direction while constructing the filament–wound structure, as illustrated in Figure 5. The corresponding first linear buckling modes are shown in Figure 18. When $\theta_1^{VP}, \theta_2^{VP}, \theta_3^{VP}$ are different within the same $\pm\theta$ layer, a variable–angle filament path is produced, which is well illustrated in some of the Figures. Due to the tow bending and tow shearing mechanisms discussed in Wang et al. [13], the variable–angle path creates overlapping regions with higher thickness between the filaments, here represented by darker regions. This coupling between the thickness and the steering angle leads to interesting optimum designs, such as the ones illustrated in Figure 13, Figure 15 and Figure 16.

For design loads that allow an optimum configuration for

Table 10
Optimization results from both PSO–MM and GA approaches.

Approach	Design Load (kN)	k_n	$\theta_1^{VP}(°)$	$\theta_2^{VP}(°)$	$\theta_3^{VP}(°)$	Mass (kg)	λ (kN)
PSO–MM	50	k_1	± 46.3	± 57.8	± 57.8	0.3704	50.31
GA	50	k_1	± 41.8	± 68.0	± 49.9	0.3888	49.99
PSO–MM	100	k_1	± 60.9	± 60.0	± 64.8	0.7291	165.33
		k_2	± 41.3	± 41.6	± 39.7		
GA		k_1	± 22.9	± 22.9	± 21.4	0.7238	288.15
		k_2	± 40.0	± 40.0	± 40.0		
PSO–MM	200	k_1	± 6.8	± 5.2	± 6.4	0.7309	207.61
		k_2	± 31.0	± 38.2	± 37.0		
GA		k_1	± 28.3	± 28.3	± 27.6	0.7238	242.83
		k_2	± 75.1	± 75.1	± 75.1		
PSO–MM	500	k_1	± 10.5	± 56.5	± 10.6	1.2715	498.29
		k_2	± 9.6	± 80.7	± 58.3		
		k_1	± 54.2	± 53.9	± 53.4	1.0951	504.28
		k_2	± 59.8	± 65.7	± 63.7		
		k_3	± 45.9	± 46.9	± 43.0		
GA		k_1	± 49.6	± 48.9	± 48.2	1.0861	659.80
		k_2	± 83.6	± 85.0	± 85.0		
		k_3	± 39.0	± 39.0	± 45.4		
PSO–MM	1000	k_1	± 72.3	± 67.5	± 6.6	1.6112	1012.51
		k_2	± 7.0	± 63.3	± 87.5		
		k_1	± 62.3	± 36.0	± 52.2	1.5877	1008.79
		k_2	± 18.0	± 74.4	± 87.1		
		k_3	± 76.5	± 85.6	± 34.4		
		k_1	± 37.3	± 37.0	± 36.2	1.4586	1092.18
		k_2	± 62.1	± 65.7	± 65.9		
		k_3	± 5.9	± 7.0	± 5.8		
		k_4	± 31.3	± 33.0	± 35.7		
GA		k_1	± 21.3	± 22.7	± 19.1	1.4487	1301.76
		k_2	± 53.9	± 48.9	± 51.0		
		k_3	± 79.4	± 78.0	± 78.0		
		k_4	± 22.7	± 19.8	± 17.7		

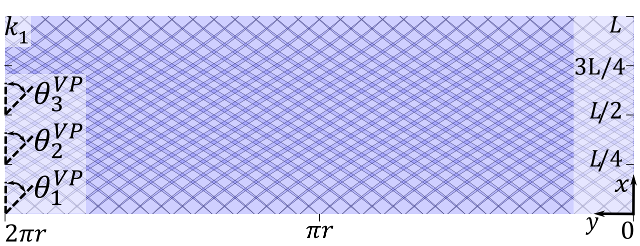

Figure 10: PSO-MM tow path for design load of 50 kN.

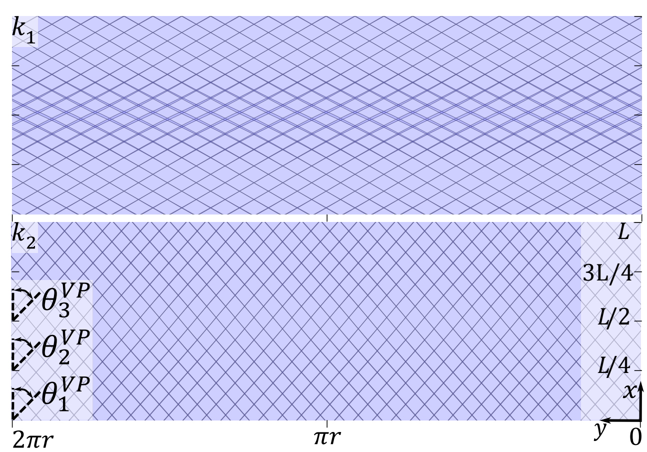

Figure 11: PSO-MM tow path for design load of 100 kN with 2 $\pm\theta$ layers.

different values of the total number of layers N_L, a general trend is observed, in which lower N_L values can achieve the design load by means of more thickness build–up created by the variable–angle filaments. On the other hand, higher N_L values tend to show less thickness build–up, thus with less variability in the filament angles. Another trend that is observed is that the buckling modes for the configurations with more thickness build–up tend to show the well-known diamond patterns, whereas the optima with more N_L have more axisymmetric buckling modes.

7. Conclusion

This work focused on develop an optimization framework coupled with metamodels to minimize the mass of variable–angle filament–wound (VAFW) cylinders. The newly pro-

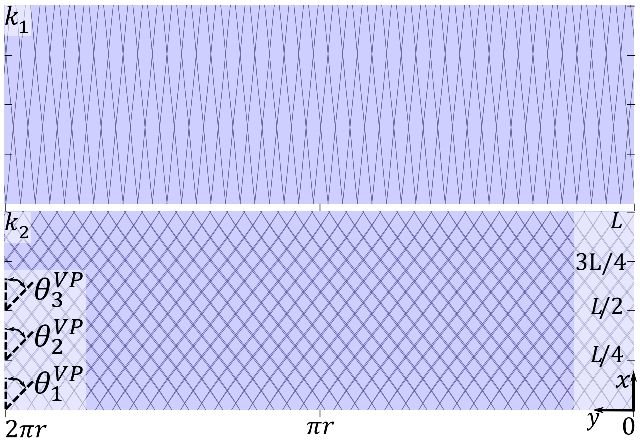

Figure 12: PSO-MM tow path for design load of 200 kN with 2 $\pm\theta$ layers.

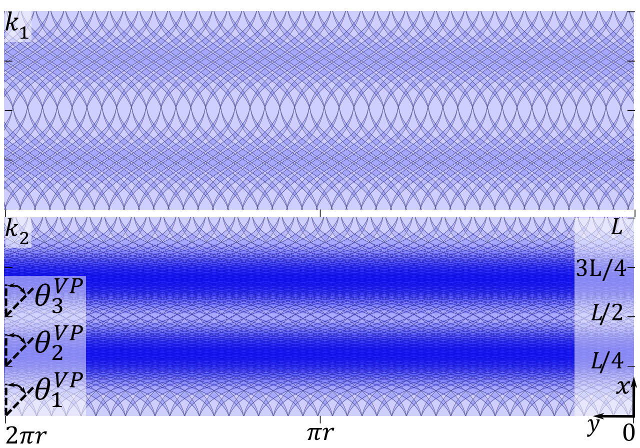

Figure 13: PSO-MM tow path for design load of 500 kN with 2 $\pm\theta$ layers.

posed single–curvature Bogner-Fox-Schmit-Castro finite element with 4 nodes and 10 degrees-of-freedom (DOF) per node showed to be a fast–converging element to simulate the buckling behavior of VAFW cylinders. The model converges with approximately two orders of magnitude less DOF than a general purpose linear shell element, such as the S4R available in Abaqus.

The accelerated Kriging metamodel used to represent the buckling behavior and the mass of VAFW cylinders proved to be accurate and could be trained using only 183 finite element evaluations. This is remarkable considering the steering–thickness coupling observed in this variable–stiffness structure. The moving search window, or hypercube, used during the training process enabled the proposed accelerated Kriging to outperform the conventional Kriging and the co-Kriging approaches.

Particle swarm optimization was successfully used to drive the trained Kriging models towards different optima for buckling design loads of 50 kN, 100 kN, 200 kN, 500 kN and 1000 kN. All optimum results were verified against genetic algorithm optimizations coupled with finite elements, showing a very good agreement in the obtained minimum

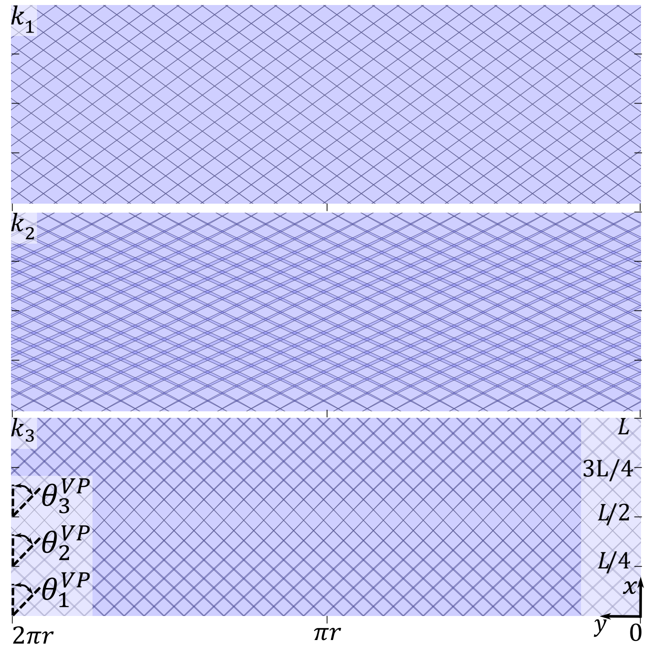

Figure 14: PSO-MM tow path for design load of 500 kN with 3 $\pm\theta$ layers.

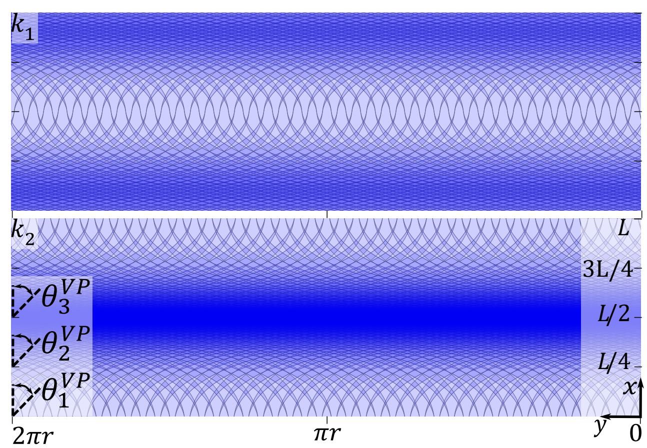

Figure 15: PSO-MM tow path for design load of 1000 kN with 2 $\pm\theta$ layers.

mass. The GA runs required above 60 generations and a total of 3841 finite element evaluations to converge.

Future studies will focus on manufacture the optimum cylinder configurations herein achieved through the filament winding process. In addition, the cylinders will be tested in axial compression and non–linear models will be developed to simulate their buckling performance.

References

[1] L. Zhu, N. Li, P. Childs, Light-weighting in aerospace component and system design, Propulsion and Power Research 7 (2) (2018) 103–119. doi:https://doi.org/10.1016/j.jppr.2018.04.001.

[2] T. R. Brooks, J. R. Martins, On manufacturing constraints for tow-steered composite design optimization, Composite Structures 204 (2018) 548–559. doi:https://doi.org/10.1016/j.compstruct.2018.07.100.

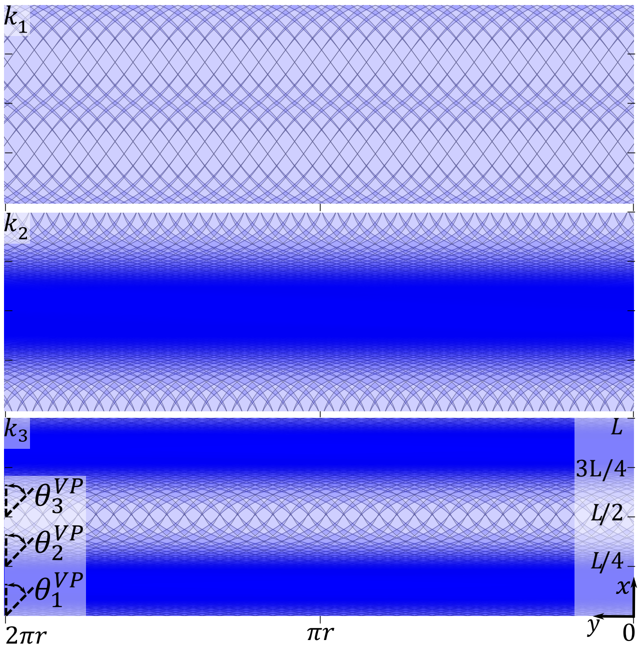

Figure 16: PSO-MM tow path for design load of 1000 kN with 3 $\pm\theta$ layers.

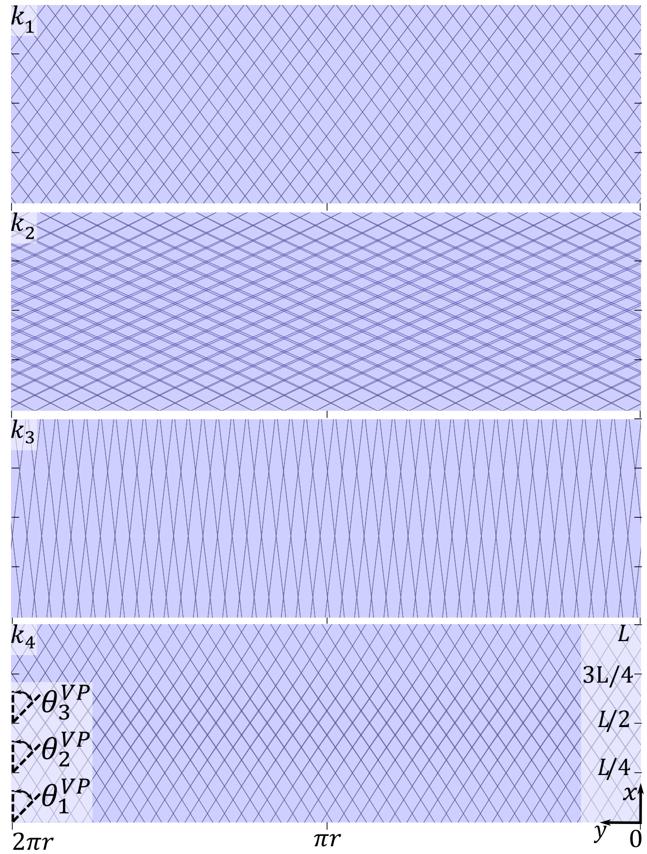

Figure 17: PSO-MM tow path for design load of 1000 kN with 4 $\pm\theta$ layers.

[3] F. S. Liguori, G. Zucco, A. Madeo, D. Magisano, L. Leonetti, G. Garcea, P. M. Weaver, Postbuckling optimisation of a variable angle tow composite wingbox using a multi-modal Koiter approach, Thin-Walled Structures 138 (2019) 183–198. doi:10.1016/j.tws.2019.01.035.

[4] M. Hyer, H. Lee, The use of curvilinear fiber format to improve buckling resistance of composite plates with central circular holes, Composite Structures 18 (3) (1991) 239–261. doi:https://doi.org/10.1016/0263-8223(91)90035-W.

[5] R. Degenhardt, S. G. Castro, M. A. Arbelo, R. Zimmerman, R. Khakimova, A. Kling, Future structural stability design for composite space and airframe structures, Thin-Walled Structures 81 (2014) 29–38. doi:10.1016/j.tws.2014.02.020.

[6] S. G. Castro, R. Zimmermann, M. A. Arbelo, R. Khakimova, M. W. Hilburger, R. Degenhardt, Geometric imperfections and lower-bound methods used to calculate knock-down factors for axially compressed composite cylindrical shells, Thin-Walled Structures 74 (2014) 118–132. doi:10.1016/j.tws.2013.08.011.

[7] J. Pelletier, S. Vel, Multi-objective optimization of fiber reinforced composite laminates for strength, stiffness and minimal mass, Computers Structures 84 (29) (2006) 2065–2080. doi:https://doi.org/10.1016/j.compstruc.2006.06.001.

[8] M. Sadeghifar, M. Bagheri, A. Jafari, Multiobjective optimization of orthogonally stiffened cylindrical shells for minimum weight and maximum axial buckling load, Thin-Walled Structures 48 (12) (2010) 979–988. doi:https://doi.org/10.1016/j.tws.2010.07.006.

[9] A. Ghasemi, M. Hajmohammad, Multi-objective optimization of laminated composite shells for minimum mass/cost and maximum buckling pressure with failure criteria under external hydrostatic pressure, Structural and Multidisciplinary Optimization 55 (2017) 1051–1062. doi:https://doi.org/10.1007/s00158-016-1559-2.

[10] M. Rouhi, H. Ghayoor, S. Hoa, M. Hojjati, Multi-objective design optimization of variable stiffness composite cylinders, Composites Part B: Engineering 69 (2015) 249–255. doi:https://doi.org/10.1016/j.compositesb.2014.10.011.

[11] A. W. Blom, P. B. Stickler, Z. Gürdal, Design and Manufacture of a Variable-Stiffness Cylindrical Shell, Tech. rep. (2009). URL https://repository.tudelft.nl/islandora/object/uuid%3A0d8a5de7-966a-4f80-bc5c-bc6bb1733410

[12] A. Booker, J. Dennis, P. Frank, D. Serafini, V. Torczon, M. Trosset, A rigorous framework for optimization of expensive functions by surrogates, Structural and Multidisciplinary Optimization 17 (1999) 1–13. doi:https://doi.org/10.1007/BF01197708.

[13] Z. Wang, J. H. S. Almeida Jr., L. St-Pierre, Z. Wang, S. Castro, Reliability-based buckling optimization with an accelerated Kriging metamodel for filament-wound variable angle tow composite cylinders, Composite Structures 254 (2020).

[14] J. H. S. Almeida Jr., M. L. Ribeiro, V. Tita, S. C. Amico, Damage and failure in carbon/epoxy filament wound composite tubes under external pressure: Experimental and numerical approaches, Materials Design 96 (2016) 431–438. doi:https://doi.org/10.1016/j.matdes.2016.02.054.

[15] S. Castro, E. Jansen, Displacement-based formulation of Koiter's method: Application to multi-modal post-buckling finite element analysis of plates, Thin-Walled Structures 159 (2021) 107217. doi:10.1016/j.tws.2020.107217.

[16] H. B. de Quadros, J. A. Hernandes, A Lagrange parametrization for the design of variable stiffness laminates, Structural and Multidisciplinary Optimization 58 (1) (2018) 129–137. doi:10.1007/s00158-017-1882-2.

[17] S. G. Castro, M. V. Donadon, T. A. Guimarães, ES-PIM applied to buckling of variable angle tow laminates, Composite Structures 209 (2019) 67–78. doi:10.1016/j.compstruct.2018.10.058.

[18] L. Vertonghen, S. G. Castro, Modelling of fibre steered plates with coupled thickness variation from overlapping continuous tows, Composite Structures (2021) 113933doi:10.1016/j.compstruct.2021.113933.

[19] F. K. Bogner, R. L. Fox, L. A. Schmit Jr., The generation of inter-element-compatible stiffness and mass matrices by the use of interpolation formulas, in: Matrix Methods in Structural Mechanics, Air-

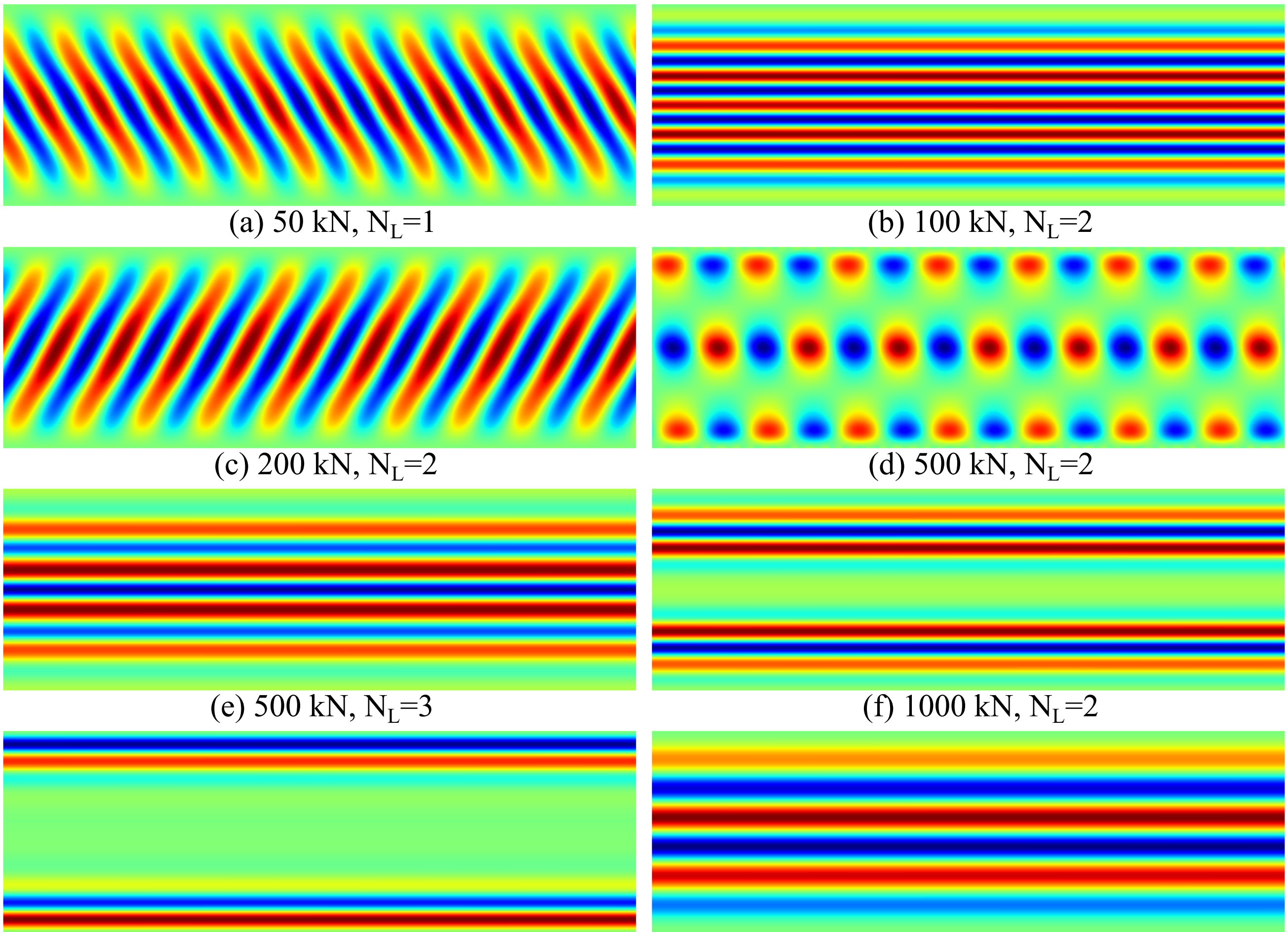

(a) 50 kN, N_L=1

(b) 100 kN, N_L=2

(c) 200 kN, N_L=2

(d) 500 kN, N_L=2

(e) 500 kN, N_L=3

(f) 1000 kN, N_L=2

(g) 1000 kN, N_L=3

(h) 1000 kN, N_L=4

Figure 18: Buckling modes for all cylinders optimized by the PSO–MM framework.

Force Inst. of Tech., Wright Patterson AF Base, Cleveland, Ohio, 1966, pp. 395–444.
URL http://contrails.iit.edu/reports/8569

[20] O. O. Ochoa, J. N. Reddy, Finite Element Analysis of Composite Laminates, Springer, Dordrecht, 1992, pp. 37–109. doi:10.1007/978-94-015-7995-7_3.
URL http://link.springer.com/10.1007/978-94-015-7995-7{_}3

[21] D. Q. Tsunematsu, The aeroelastic behavior of laminated composite panels undergoing progressive damage in supersonic flow, Thesis of doctor of science, Instituto Tecnológico de Aeronáutica (2019).

[22] D. Q. Tsunematsu, M. V. Donadon, Aeroelastic behavior of composite panels undergoing progressive damage, Composite Structures 210 (2019) 458–472. doi:10.1016/J.COMPSTRUCT.2018.11.065.
URL https://www.sciencedirect.com/science/article/pii/S0263822318314508{#}b0110

[23] E. J. Barbero, J. N. Reddy, J. L. Teply, General two-dimensional theory of laminated cylindrical shells, AIAA Journal 28 (3) (1990) 544–553. doi:10.2514/3.10426.

[24] J. N. Reddy, Mechanics of Laminated Composite Plates and Shells, 2nd Edition, CRC Press, 2003. doi:10.1201/b12409.

[25] L. Donnell, Stability of Thin-walled Tubes under Torsion, Tech. Rep. 479, NACA Report No. 479 (1933).

[26] L. H. Donnell, A new theory for the buckling of thin cylinders under axial compression and bending, Trans. ASME 56 (11) (1934) 795–806.

[27] S. Castro, C. Mittelstedt, F. Monteiro, M. Arbelo, G. Ziegmann, R. Degenhardt, Linear buckling predictions of unstiffened laminated composite cylinders and cones under various loading and boundary conditions using semi-analytical models, Composite Structures 118 (2014) 303–315. doi:https://doi.org/10.1016/j.compstruct.2014.07.037.

[28] A. V. Knyazev, Toward the Optimal Preconditioned Eigensolver: Locally Optimal Block Preconditioned Conjugate Gradient Method, SIAM Journal on Scientific Computing 23 (2) (2001) 517–541. doi:10.1137/S1064827500366124.

[29] P. Virtanen, R. Gommers, T. E. Oliphant, et al., SciPy 1.0: Fundamental Algorithms for Scientific Computing in Python, Nature Methods 17 (2020) 261–272. doi:10.1038/s41592-019-0686-2.

[30] M. Smith, ABAQUS/Standard User's Manual, Version 2019, Dassault Systèmes Simulia Corp, United States, 2019.

[31] A. I. Forrester, A. Sóbester, A. J. Keane, Multi-fidelity optimization via surrogate modelling, Proceedings of the Royal Society A: Mathematical, Physical and Engineering Sciences 463 (2088) (2007) 3251–3269. doi:10.1098/rspa.2007.1900.
URL https://royalsocietypublishing.org/doi/10.1098/rspa.2007.1900

[32] S. N. Lophaven, DACE - A Matlab Kriging Toolbox, Version 2.0 (2002).

[33] Q. Zhou, Y. Wu, Z. Guo, J. Hu, P. Jin, A generalized hierarchical co-kriging model for multi-fidelity data fusion, Structural and Multidisciplinary Optimization 62 (2020) 1885–1904. doi:https://doi.org/10.1007/s00158-020-02583-7.

[34] J. Kennedy, R. Eberhart, Particle swarm optimization, in: Proceedings of ICNN'95 - International Conference on Neural Networks,

Vol. 4, IEEE, 1995, pp. 1942–1948. doi:10.1109/ICNN.1995.488968.

[35] J. Gray, J. Hwang, J. Martins, K. Moore, B. Naylor, OpenMDAO: An open-source framework for multidisciplinary design, analysis, and optimization, Structural and Multidisciplinary Optimization 59 (4) (2019) 1075–1104. doi:10.1007/s00158-019-02211-z.